공학박사 학위논문

Study on irreversible degradation mechanism of organic-inorganic hybrid perovskite materials by trapped charges

갇힌 전하에 의한 유무기 페로브스카이트 물질의 비가역적인 분해 현상 연구

2019 년 2 월

서울대학교 대학원

기계항공공학부

곽 귀 성

갇힌 전하에 의한 유무기 페로브스카이트 물질의 비가역적인 분해 현상 연구

Study on irreversible degradation mechanism of organic-inorganic hybrid perovskite materials by trapped charges

지도교수 최 만 수

이 논문을 공학박사 학위논문으로 제출함

2018 년 10 월

서울대학교 대학원

기계항공공학부

곽 귀 성

곽귀성의 공학박사 학위논문을 인준함

2018 년 12 월

위 원 장	이 윤 석	(인)
부위원장	최 만 수	(인)
위 원	남 기 태	(인)
위 원	정 현 석	(인)
위 원	김 상 문	(인)

Study on irreversible degradation mechanism of organic-inorganic hybrid perovskite materials by trapped charges

Kwisung Kwak
School of Mechanical and Aerospace Engineering
The Graduate School
Seoul National University

Abstract

Organic-inorganic hybrid perovskite crystal has excellent photo-electronic properties, so it is used as various photo-electronic devices. In particular, organic-inorganic hybrid perovskite solar cells are expected to replace silicon solar cells because of their high efficiency and low production costs. The biggest problem of commercialization of organic-inorganic perovskite solar cell is low stability. There are various reasons for the lack of stability of the perovskite solar cell, but the most important reason is that the perovskite material is easily decomposed when light is irradiated in air. In addition, perovskite material is degraded by various factors. Therefore, it is

essential to clarify the origin and decomposition process of irreversible degradation of perovskite materials to ensure long-term stability of perovskite solar cells.

First, the degradation of $CH_3NH_3PbI_3$ ($MAPbI_3$) material, which is most commonly used in perovskite solar cells, was studied. In the case of perovskite solar cells, efficiency, hysteresis, and degradation patterns were different depending on the electron transport layer. It is assumed that the origin of the degradation of the perovskite materials is charge because it is a characteristic occurred by the behavior of charges. To demonstrate the effect of charges, a corona discharge method was used to inject charges without light irradiation. The transfer of the charges injected by the corona discharge method to the perovskite layer was confirmed by using Kelvin Probe Force Microscopy (KPFM) and PL (Photoluminescence) spectroscopy. The perovskite material was decomposed under the conditions of the injected charge and water or oxygen. These results demonstrate that the trapped charges in the perovskite are the origin of the decomposition of the perovskite material. In order to analyze the theoretical decomposition mechanism of perovskite materials, the ab initio molecular dynamics (AIMD) simulation based on density functional theory (DFT) was carried out. As a result of the simulation, when the trapped charges were present, it was observed that the perovskite crystal collapsed by reacting with moisture or oxygen, but there was nothing happened without the trapped charges.

Second, the investigation of different composition of perovskite material and its degradation mechanism were studied. The crystal structure can be

changed from tetragonal structure to a cubic structure by changing the organic cation or halide anion in $MAPbI_3$ through the calculation of the goldschmidt tolerance factor. In the case of the cubic structure, the structural stability is superior to the tetragonal structure and high efficiency can be obtained. Therefore, the perovskite composition which has the cubic structure was investigated using $CH((NH_2)_2)^+$ (FA^+) organic cation instead of $CH_3NH_3^+$ (MA^+) organic cation and Br^- halide anion instead of I^- halide anion. As a result, we found the composition of $MA_{0.6}FA_{0.4}PbI_{2.9}Br_{0.1}$, which has an efficiency of 20.2% and superior stability to $MAPbI_3$. This composition also was decomposed in the presence of trapped charge, but it showed high stability in oxygen atmosphere compared with $MAPbI_3$.

Recently, $FAPbI_3$ material, which has cubic structure, has been widely used because of its high light absorption properties and excellent light stability. However, since the stability of $FAPbI_3$ material is also not sufficient for commercialization, the degradation mechanism of $FAPbI_3$ material was studied. In the case of $FAPbI_3$, it was confirmed that it rapidly changed from a cubic structure to a hexagonal structure under high relative humidity condition. However, when oxygen was injected under the light irradiation condition, it was confirmed that the crystal was decomposed into PbI_2. This process was also confirmed by the corona discharge method and the AIMD simulation

Keywords: perovskite solar cell, organic-inorganic hybrid perovskite, trapped charge, electron transport layer, degradation mechanism, corona discharge, AIMD simulation, cubic structure, mixed compositional perovskite,

Student Number: 2013-20643

Contents

List of Tables

Nomenclature

V_{oc}	out-circuit voltage	[V]
J_{sc}	short-circuit current density	[mA cm^{-2}]
U_{offset}	Offset voltage for suppression charge extraction	[V]
U_{max}	Maximum voltage	[V]
j_0	Capacitive displacement current	[mA cm^{-2}]
A	Voltage increase rate	[V/s]
t_{max}	Time at maximum current	[s]
μ	Carrier mobility	[cm^2 $V^{-1}s^{-1}$]
r_A	Radius of A site cation	[nm]
r_x	Radius of X site anion	[nm]
r_{Pb}	Radius of Pb^{2+}	[nm]
t	Goldschmidt tolerance factor	

List of Figures

Chapter 1. Introduction

1.1. Research Background

Research on renewable energy for replacing petroleum energy is very active worldwide. Although there are many types of renewable energy, the demand for solar cells using infinite solar energy is continuously increasing.[1] Currently, the solar cell industry is dominated by Si-based solar cells. However, these are many disadvantages in Si-based solar cell, for example expensive production cost, so many researchers are studying various next-generation solar cells which can replace Si-based solar cells.

Among the next generation solar cells, perovskite solar cells have recently been shown to be the most promising solar cells to replace Si-based solar cells, with a remarkably high efficiency of more than 23%. These perovskite solar cells have shown very rapid efficiency growth since their first reported in a group of prof. Miyasaka in 2009.[2] $CH_3NH_3PbI_3$ ($MAPbI_3$) material is the most widely used and studied material in the study of perovskite solar cells. $MAPbI_3$-based perovskite solar cells has been studied very actively because it is easy to manufacture and shows about 20% efficiency.[3] In addition, $MAPbI_3$-based perovskite solar cells can be processed at

under 150℃, and they are still widely used in various photo-electronic devices such as flexible devices.[4] In recent years, in order to achieve higher efficiency, mixed composition perovskite solar cells using a mixture of various organic cations instead of $MAPbI_3$ have been studied.[5-7] Among these various composition perovskite solar cells, $CH((NH)_2)_2PbI_3$($FAPbI_3$)-based perovskite solar cells are also vigorously studied because they show high power conversion efficiency and excellent light and thermal stability. [8,9]

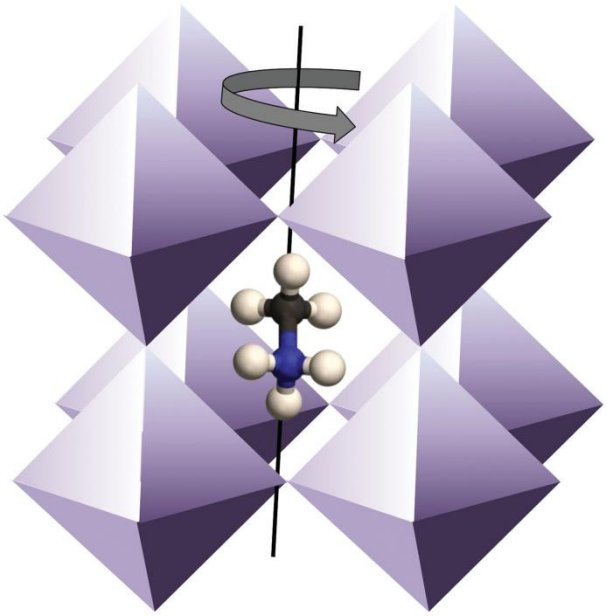

Figure 1.1 Schematic image of perovskite crystal structure adopted from [10].

1.1.1. The stability of $MAPbI_3$ perovskite materials.

Despite of rapid efficiency growth, perovskite solar cells still fail to commercialize because the stability of perovskite is very poor. Although perovskite solar cells have been reported to have stability over 1000 hours in recent years,[11] they have not yet achieved sufficient stability for commercialization. There are many reasons why the efficiency of perovskite solar cells is diminishing. Many studies have been reported that the stability of the charge transport layer constituting the perovskite solar cell and the migration of metal electrode affect the stability of perovskite solar cells.[12-14] But the biggest problem is that the stability of perovskite material itself is poor.[15-17] In particular, the stability of $MAPbI_3$ material, which is the most frequently used, is very terrible, and therefore, the efficiency of a $MAPbI_3$-based perovskite solar cells is widely known to decrease rapidly in a short time.[17,18] The $MAPbI_3$ material is easily transformed into PbI_2 due to the collapse of the crystal structure.[17]

There were studies to investigate the causes of degradation of $MAPbI_3$ perovskite materials as seen in Figure 1.1. First, there is a reversible hydration state due to moisture.[15,19] In the case of the $MAPbI_3$ material, it becomes a hydration state($CH_3NH_3PbI_3 \cdot H_2O$ or $(CH_3NH_3)_4PbI_6 \cdot 2H_2O$) in combination with moisture under a high

relative humidity environment. The hydration state of $MAPbI_3$ has a transparent color, which means that it cannot absorb the light. Therefore, the hydration state of $MAPbI_3$ materials does not function as a light absorber, and thus the solar cell is not driven. This transparent hydration state return to its original black perovskite state in the absence of moisture, but it does not act as a solar cell during the hydration state.

Next, photo-degradation by photocatalytic effect under light illumination was reported in a group of prof. Ito.[20] When the electron transport layer is made of TiO_2, TiO_2 absorbs light under light illumination condition, and the photocatalytic effect of TiO_2 destroys $MAPbI_3$ into PbI_2. Recently, perovskite solar cells using different types of electron transport layers have been reported to replace TiO_2.[21,22]

The degradation by strong electric field was by a group of Petrozza and Snaith.[23] After deposition of two au electrodes on the perovskite surface, the application of a strong electric field between the two electrodes causes degradation from near the electrodes. At this time, the electric field applied between the two electrodes is about 600 V / cm, and they said that the strong electric field causes the migration of organic cations and finally the perovskite crystals collapse.

The group of prof. Haque reported that degradation of $MAPbI_3$ material occurs when light is irradiated in an oxygen atmosphere.[16,24,25] When light is irradiated on $MAPbI_3$, excited electrons are generated. As the electron is transferred to oxygen, the oxygen becomes a superoxide state, and this superoxide decomposes $MAPbI_3$ material. In particular, during the $MAPbI_3$ degradation process, they speculated the deprotonation of organic cation. The hydrogen atoms in $MAPbI_3$ are separated and combine with oxygen to form water, and $MAPbI_3$ decomposed into PbI_2.

In addition, a variety of causes have been identified as the origin of the degradation of $MAPbI_3$. However, it is unclear what process $MAPbI_3$ material will undergo during the degradation.

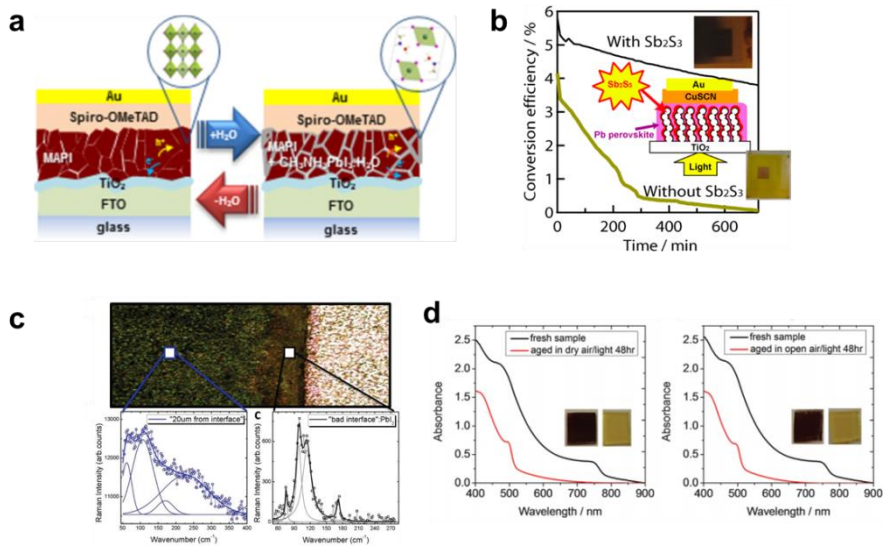

Figure 1.2 (a) Schematic of reversible hydration formation of $MAPbI_3$ material adopted from [15]. (b) Degradation of $MAPbI_3$ material by photo catalytic effect of TiO_2 adopted from [20] (c) Ion migration driven degradation of $MAPbI_3$ material by electric field adopted from [23] (d) Decomposition of $MAPbI_3$ material by super oxide generated under oxygen ambient adopted from [24].

1.1.2. The stability of $FAPbI_3$ perovskite materials

Recently, the perovskite solar cells using black alpha phase $FAPbI_3$ (α-$FAPbI_3$) material as a light absorber have been reported in recent years.[8,9] α-$FAPbI_3$ material has higher light absorption efficiency and light and thermal stability than $MAPbI_3$. However, pureα-$FAPbI_3$ material is unstable in the presence of water at room temperature. Because the Goldschmidt tolerance factor of pure $FAPbI_3$ is greater than 1 at room temperature, this means that the hexagonal delta phase $FAPbI_3$(δ -$FAPbI_3$) is more favorable than cubic alpha phase $FAPbI_3$. (The structure of $FAPbI_3$ shown in Figure 1.3) Especially, α-$FAPbI_3$ is very vulnerable to moisture, so it changes very easily into δ -$FAPbI_3$ in the presence of water. The δ -$FAPbI_3$ material is yellowish, so it cannot act as a light absorber. Recently, it has been reported that α -$FAPbI_3$ material is maintained more stable in the presence of water at room temperature when a small amount of Cs cation enter the $FAPbI_3$ crystal structure.[8]

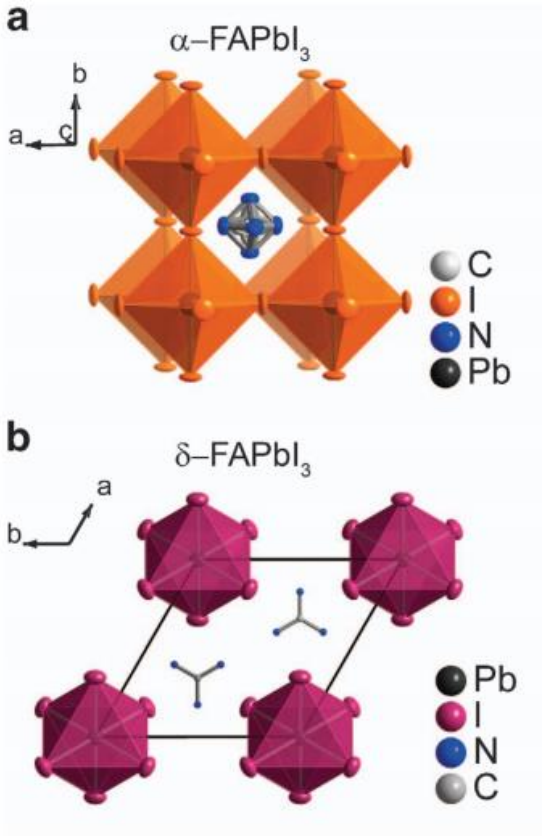

Figure 1.3 Schematic illustrations of two phases of $FAPbI_3$ material adopted from [26]. (a) α-$FAPbI_3$ have the cubic perovskite structure. (b) δ -$FAPbI_3$ have 1-Dimensional hexagonal structure.

1.1.3. Enhanced stability achieved by changing the charge extraction layer

It is well known that the efficiency and stability of perovskite solar cells depend on the charge extraction layer. Therefore, it is very important to use an appropriate charge extraction layer for the perovskite solar cells.

The prof. Han's group reported the perovskite solar cell using Nb doped TiO_x electron transporting layer. (shown in Figure 1.4 a) In this device, the rapid electron extraction were achieved by fabrication of 10-20nm of Nb doped TiO_x on the PCBM. As the result, a solar cell having no hysteresis and having higher efficiency and stability was fabricated.

In prof. Seok's group, La-doped $BaSnO_3$ was used as an electron transporting layer instead of TiO_2. (shown in Figure 1.4 b) In case of $BaSnO_3$, it has excellent electrical mobility, so charge extraction is easy and therefore it shows high stability.

In prof. Yang's Group, all charge extraction layers were made of inorganic material to improve stability. In this case, the charge extraction efficiency was much lower than that of the organic material, but the stability was much better. This is because the use of an inorganic transport layer prevents penetration of the air into the perovskite layer, thereby preventing the perovskite from being

decomposed.

Two factors play an important role in the stability of the perovskite solar cell. The first is to efficiently extract the charge from the device. The higher the extraction efficiency of the charge, the more stable the device is. Secondly, it prevents the infiltration of the air. It is very important to shut off this outside air because the air, especially moisture or oxygen, has a direct effect on the perovskite material. From these results, it can be predicted that an important factor in the decomposition phenomenon of perovskite materials is the reaction of charge and moisture or oxygen.

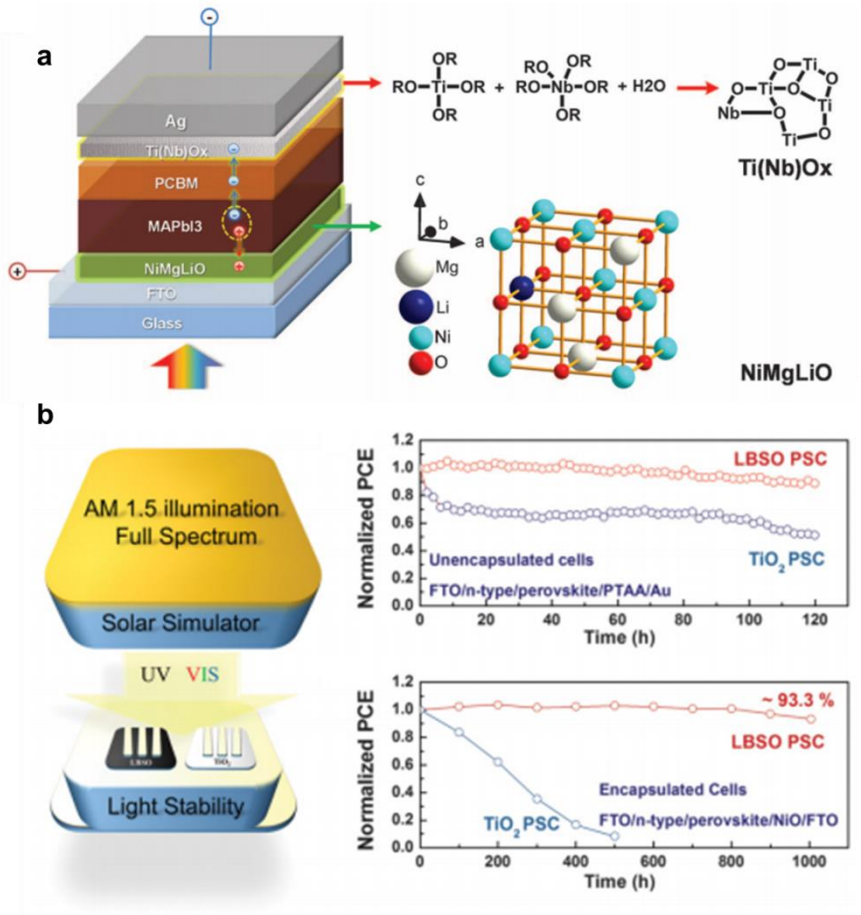

Figure 1.4 (a) Schematic illustration of the device configuration using the doped charge carrier extraction layers adopted from. [27] (b) Long-term stability of perovskite solar cells using doped electron extraction layer adopted from [28].

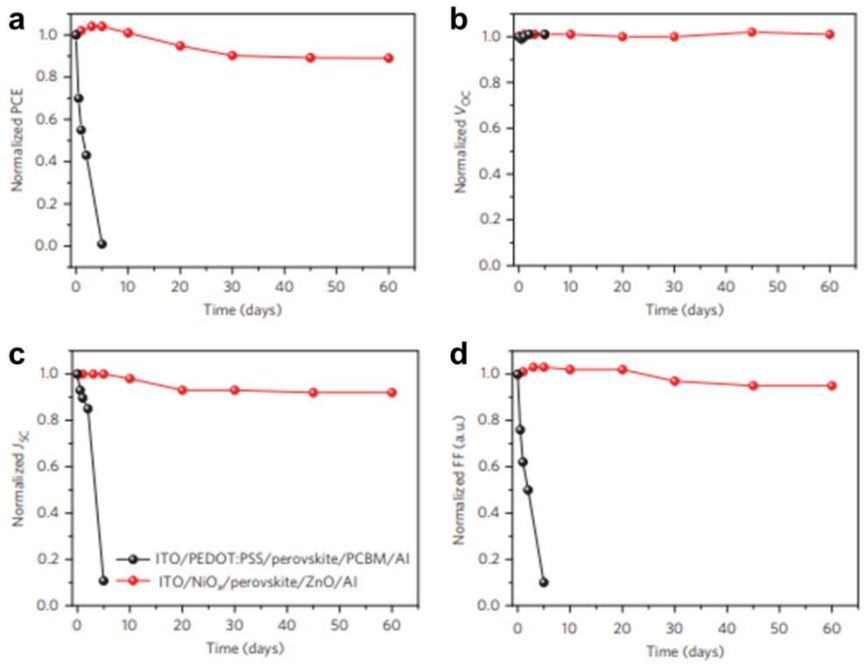

Figure 1.5 Comparison of the stability of devices based on inorganic charge extraction layer and organic charge extraction layer adopted from [29].

1.2. **Research objectives**

The dissertation aims to clarify the causes of the degradation of perovskite materials more clearly.

As seen in Table1.1, when light was illuminated in the presence of moisture or oxygen, and electric field was applied to the perovskite films between gold two electrodes in humid air, the irreversible degradation of perovskite materials occurred. Light illumination and electric field have one common point. Those are associated with charges. In other words, charges can be generated by light illumination and an electrical current through perovskites. From these results, it can be inferred that charges could be the key cause that initiates an irreversible degradation of perovskite materials. To demonstrate this speculation, a novel experimental setup was introduced and a density functional theory(DFT)-based ab initio molecular dynamics(AIMD) simulation was performed to predict a more theoretically accurate mechanism.

First, the degradation of $MAPbI_3$ material was studied. It was founded that trapped charges are the key cause of the degradation of the perovskite solar cells. When the electron transport layer was changed from TiO_2 to C_{60}, the degradation rate and degradation pattern were completely different. It was also confirmed that the hysteresis of the devices depends on the type of electron transport

layer, which means that there are accumulated charges in the perovskite layer. To demonstrate this trapped charge driven mechanism, a novel experimental device for intentionally trapping charges on the surface of perovskite was introduced. A corona discharge method was used to inject charges on the surface of perovskite layer without light irradiation. It was confirmed that the charges injected by corona discharge method or charges generated by the light are collected at the grain boundaries and some spot of grain surface by Kelvin Probe Force Microscopy(KPFM) measurement. It was also confirmed that the decomposition of perovskite material occurs when there are trapped charges in the presence of water or oxygen. The AIMD simulation based on the DFT calculation was used to clarify the degradation mechanism by the trapped charge.

Second, the search and the degradation mechanism of perovskite materials other than $MAPbI_3$ were studied. $MAPbI_3$ has a tetragonal structure so it is structurally unstable. To overcome this structure instability, it is necessary to search for perovskite materials having a cubic structure. As the Goldschmidt tolerance factor approaches 1, the perovskite crystal structure becomes closer to the cubic structure. In the case of $MAPbI_3$, since the size of $CH_3NH_3^+(MA^+)$ cation is small, it has tetragonal structure. If MA^+ cation is replaced with $CH((NH_2)_2)^+(FA^+)$ cation, the perovskite crystal structure can be

close to cubic structure. As the result of stability and efficiency of various composition perovskite material, $MA_{0.6}FA_{0.4}PbI_{2.9}Br_{0.1}$ showed best stability and showed 20.2% of power conversion efficiency. However, $MA_{0.6}FA_{0.4}PbI_{2.9}Br_{0.1}$ material also was degraded in the presence of trapped charge and water molecule.

Finally, the degradation mechanism ofα-$FAPbI_3$ perovskite material was studied.. In the case of α-$FAPbI_3$, it was found that it easily changed into delta phase under high water conditions. However α-$FAPbI_3$ material did not changed into delta phase but was decomposed into PbI_2. This degradation mechanism was also identified through AIMD simulation.

	Light on	Light off	Electric field
Nitrogen	No degradation	No degradation	-
Water	Irreversible degradation	Reversible degradation	Irreversible degradation
Oxygen	Irreversible degradation	No degradation	-

Table 1.1 Summary of the causes of the degradation of perovskite material according to previous reports.

Chapter 2.

Trapped charge driven degradation of $CH_3NH_3PbI_3$($MAPbI_3$) material.

Published in *Nature Communications*, 2016, **7**, 13422

Updated in arXiv:1709.04130

2.1. Introduction

Metal halide perovskites have been attracting worldwide interest and the power conversion efficiency (PCE) of perovskite based solar cells has already exceeded 22%. Their long-term stability issue is the most pressing problem for commercialization.[18] It is well known that perovskite materials are vulnerable to the exposure of humidity and light.[19,30,31] Though many efforts to encapsulate the devices for preventing direct contact to humidity have been attempted, it was not successful to obtain long-term stability comparable to commercial photovoltaic devices.[27] Various factors that can affect the stability have been investigated from the viewpoints of chemical structure[32], electrical stress[23], hydrated states[15,19,30] and heat[33]. However, the degradation mechanism is still unclear how a

fully fabricated device deteriorates rapidly even though its perovskite layer is tightly-covered by the hole transport material(HTM) and the back electrode. It is also elusive why light soaking causes irreversible degradation of perovskite materials in the presence of moisture while the moisture in the dark condition only induces reversible hydration of perovskite materials.[23,30]

The device structure and the choice of charge extraction materials also influence the stability. The use of inorganic charge extraction layers was reported to enhance stability.[11,27] Other studies have focused on eliminating the pathway of water vapor infiltration into the perovskite film by coating carbon-based materials, polymers, and hydrophobic materials on the top surface of the perovskite film.[31,34] These approaches provide the device lifespan longer than the case without these materials, but not long enough to ensure long-term stability. Such approaches also occasionally sacrifice the photovoltaic performance. Especially, the devices employing titanium dioxide (TiO_2) as electron transport layer(ETL) are rapidly degraded under light soaking[8] even though they are highly efficient in energy conversion and exhibit the world's best efficiency.

In the present study, we demonstrate that the charges trapped at the interface between perovskite and charge extraction materials are responsible for the irreversible degradation due to moisture. The

elusive experimental puzzles both on the occurrence of degradation beginning from different side depending on different charge extraction material and the role of light soaking for irreversible degradation will be clearly explained from the present concept of the trapped charges later.

We also experimentally demonstrate that trapped charges also induce irreversible degradation of $MAPbI_3$ even in the absence of moisture as long as oxygen is supplied. These results suggest that the trapped charges lead to the degradation of perovskite material when there is oxygen or water or both. In our experiments, charges were generated either by light soaking or corona ion deposition[35], and trapped charges on the grain boundaries were confirmed by Kelvin Probe Force Microscopy (KPFM) measurements for either case of light soaking or ion deposition. To investigate the details of charge-driven degradation mechanism at the atomic level, we carried out AIMD simulations and tracked how oxygen and water molecules in the presence of trapped charges interact with the compositional units of $MAPbI_3$ crystal in the first 2 ps. From these calculations, we confirmed that deprotonation of organic cations could be induced by trapped charges in the presence of water. We also learned that oxygen molecules greatly weaken the $MAPbI_3$ crystal bonding when there are trapped charges even without water.

2.2. Results and discussion

First, we examined how solar cell degradation behavior becomes different depending on different charge extraction layers, for example, C_{60} and compact TiO_2.

As shown in Figure 2.1a, b, non-encapsulated C_{60} based cell shows much more stable performance under one sun illumination but still degrades while compact TiO_2 based non-encapsulated cell completely died only after 6 hours. To examine the detailed evolution of degradation, we investigated how the cross sectional morphology of the C_{60} and TiO_2 based devices would evolve under illumination via the focused ion beam (FIB) assisted scanning electron microscope (SEM) images shown in Figure 2.1c, d. Consistent with the PCE measurement results, the SEM images clearly confirm that the C_{60}-based devices are much slowly degraded compared to the TiO_2-based cells. Strikingly, they showed different degradation patterns, namely, different side of degradation beginning where the degradation is initiated depending on different ETLs.

Since the reactants that can decompose perovskite materials could infiltrate from the thin metal electrode rather than from the thick ITO glass, it would be expected that the degradation should be initiated at the interface closer to the thin Au metal electrode. However, the perovskite films of TiO_2-based devices began to be decomposed at

the interface adjacent to the compact TiO_2 layer near FTO glass (as shown in **Figure 2.1d**). Although these observations were attributed to UV light induced photocatalytic effect of TiO_2 layer according to the previous report[20], we confirmed that the same degradation pattern happened in the TiO_2 and C_{60} based devices aged even under UV-filtered light illumination (see **Figure 2.2**).For those of C_{60}-based devices, the decomposition began from the interface adjacent to HTL near Au metal electrode opposite to the case of TiO_2 based devices. Since the two types of devices have identical structure except for the ETL, C_{60} or TiO_2/Perovskite/Spiro-MeOTAD/Au, these different degradation characteristics indicate that charge extraction may play an important role where moisture driven decomposition of perovskite material begins.

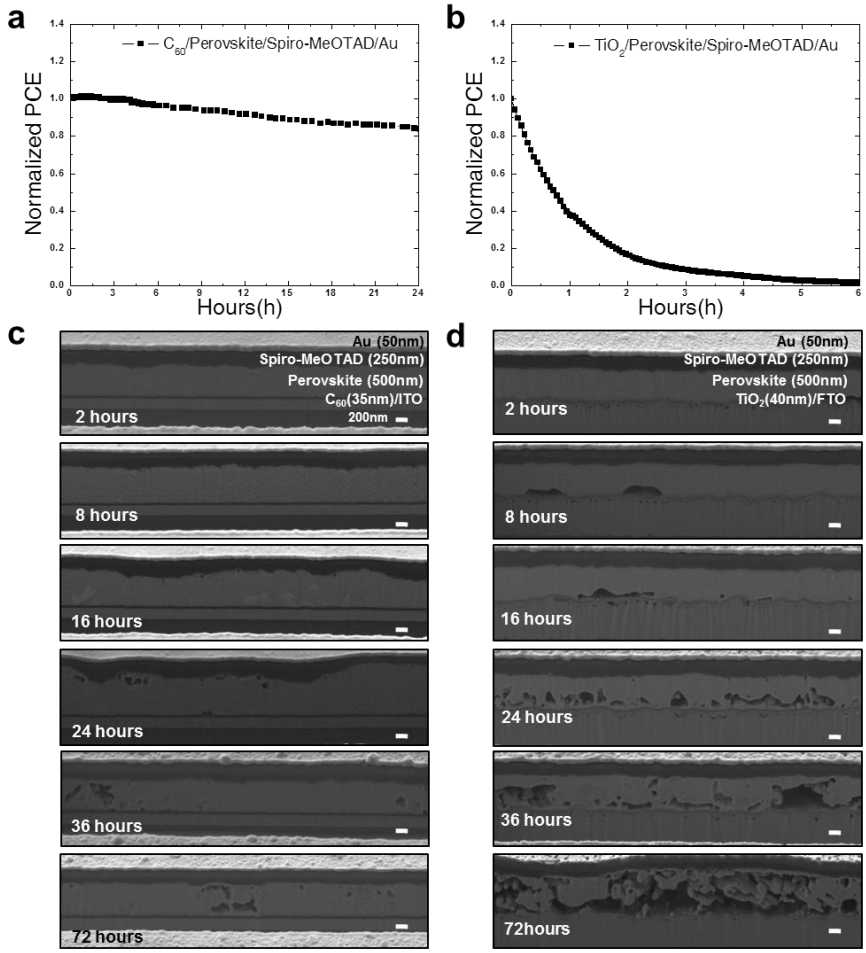

Figure 2.1 (a,b) Time evolution of the normalized PCE measured under one sun illumination in ambient conditions (relative humidity = 30%) of the (a) C60 and (b) TiO2 based devices. (c,d) Time evolution of the FIB-SEM cross-sectional images of the (c) C60 and (d) TiO2 based devices aged for 72 h under light illumination in ambient conditions. Scale bars = 200 nm.

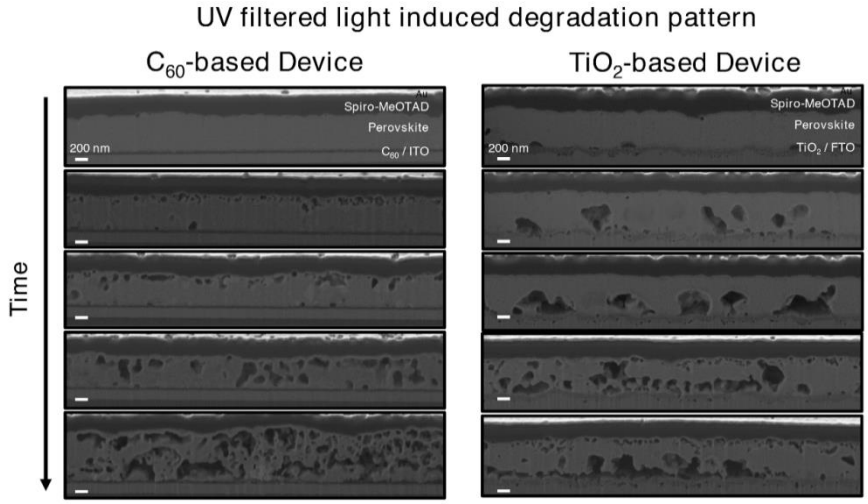

Figure 2.2 Time evolution of the FIB-SEM cross-sectional images of the C_{60} (left) and TiO_2 (right) based devices, which were aged for 48 h under UV filtered light illumination in ambient conditions. Scale bars = 200 nm.

Second, the TiO_2 based devices suffer from severe hysteresis, whereas the C_{60} based devices do not. Considering that the origin of hysteresis is known as capacitive current[36], trapped charge[37] and unbalanced charge injection[38], many electrons may be accumulated near the ETL in the TiO_2 based devices, while the C_{60} based devices hardly do. From the observation on the degradation of the TiO_2 based devices that begins from the interface contacting TiO_2 layer where many charges could be trapped, it is reasonable to suspect that trapped charges at the interface between perovskite and charge extraction layer would be responsible for initiating the moisture related decomposition. Fast extraction of electrons through C_{60} would hardly accumulate negative charges at the interface between perovskite and C_{60}, but hole extraction through Spiro-MeOTAD could be slower than the rate of electron extraction in the C_{60} based cell.[39,40] This could result in positive charge trapping at the interface between perovskite and hole extraction layer, which could be the cause why the degradation begins from the interface between perovskite and Spiro-MeOTAD for C_{60} based cells (see Figure 2.1c). These results demonstrating the degradation beginning from opposite side for different charge extraction layers gave us a clue about the trapped charge driven degradation regardless of polarity.

Another intriguing experimental observation is the light soaking in the presence of moisture which consistently showed irreversible degradation of perovskite in previous works[18,30,31] while in the dark condition moisture introduction only formed reversible hydrates of perovskites, for example, $CH_3NH_3PbI_3 \cdot H_2O$ or $(CH_3NH_3)_4PbI_6 \cdot 2H_2O$.[23,30] The reason has not been elucidated yet although Christians et al.[30] suggested that organic cation could become less tightly bound to PbI_6^{4-} octahedra after light soaking. In the present study, along with the scenario of the above mentioned trapped charges that could trigger irreversible degradation, the charge generation under light soaking and subsequent trapping on the surface of perovskite is suspected to initiate the moisture induced irreversible degradation under light illumination. To confirm the irreversible degradation under light soaking, we also investigated the experiments under light soaking or not in the presence of moisture. . Figure 2.3a showed the degradation behavior of $MAPbI_3$ for two days in the dark condition with relative humidity (RH) 90 %. Absorption spectra measurements show that the original MAPbI3 (black curve) became hydrated (red curve) after two days and then dehydrated reversibly via N_2 drying, which is consistent with previous studies.[23,30] However, $MAPbI_3$ showed irreversible degradation rapidly under light soaking even at low RH 20 % (see

Figure 2.3b), which is also consistent with previous report.[30,31,39]

As mentioned earlier, perovskite absorbing light can generate and store charges due to its capacitive property[41] that may be trapped on the grain boundaries (we will show trapped charges along grain boundaries after light soaking later). It could be hypothesized that these trapped charges generated under light soaking would be responsible for irreversible degradation, which is in line with the aforementioned hypothesis of trapped charge driven degradation explaining the initiation of degradation on different side depending on different charge extraction layers.

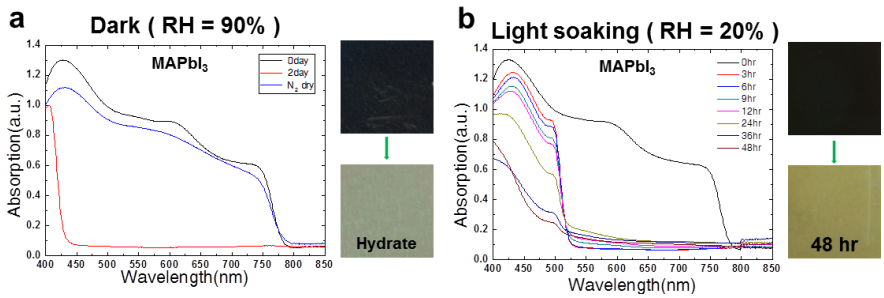

Figure 2.3 (a) Absorption spectra of $MAPbI_3$ perovskite films under dark conditions at 90% relative humidity. $MAPbI_3$ perovskites were transformed into transparent hydrated states after 2 days. (b) Time evolution of absorption spectra of $MAPbI_3$ during light soaking at 20% relative humidity. Pictures of the perovskite films before and after aging are shown on the right side of each figure.

To prove this compelling hypothesis of trapped charge driven degradation, we have configured a novel experimental setup employing an ion generator by corona discharge and a stainless chamber that blocks all incident light from outside as shown in Figure 2.4a. The air inside the chamber is isolated from the outside and controlled by two gas inlets that are connected to the independent gas sources (Gas 1 and Gas 2) (see more details in Experimental methods: Experimental setup for ion generation and deposition). Gas 1 is ionized by applying a high voltage to the pin of the corona chamber, delivered to the deposition chamber by gas flow, and deposited on the perovskite film placed at the bottom of the deposition chamber. Gas 2 passes through a water bubbler to regulate the humidity level in the deposition chamber. We measured the time evolution of the absorption spectra as the perovskite films were gradually degraded in the deposition chamber. Gas 1 was chosen as nitrogen or hydrogen for generating positive or negative ions for being used as different polarity charges trapped on the surface of perovskite, respectively while Gas 2 was nitrogen (see more details in Experimental methods: Corona ion generation). First, we needed to check that N_2 positive ions and H_2 negative ions themselves do not affect the degradation without moisture (see Figure 2.5). Next, we examined the degradation behavior in the presence of moisture when

charged ions deposited on the surface of perovskite. When the positively charged N_2 ions were deposited and the relative humidity in the chamber was held at 40%, the perovskite film rapidly decays as shown in Figure 2.4b1. The deposition of negatively charged H_2 ions also showed the similar irreversible degradation behavior under the same moisture level in Figure 2.4b2. Although Figure 2.4b2 for negative charges appears to cause slower degradation than the case shown in Figure 2.4b1 for positive charges, this could not tell which polarity charges affect more adversely on the degradation since ion generation for different polarity in our experiment is different (see more details in Experimental methods : Corona ion generation). This suggests that the irreversible degradation of perovskite materials only take place when both moisture and charges exist simultaneously. Based on these observations, the degradation mechanism could be thought of two-step process: the formation of hydrated perovskite by humidity and the irreversible decomposition by trapped charges. The first step of the formation of hydrated perovskite was already reported by several groups.[19,30] Here, we suggest that local electric field caused by trapped charge could distort electrostatically the structure of hydrated perovskite in which octahedral PbX_6^{4-} interacts with both organic cation and H_2O and trigger the initiation of irreversible decomposition of perovskite (will discuss more

complete scenario later). Leijtens et al.[23] found the irreversible degradation near the gold electrodes coated on perovskite film by applying a weak external field of 600 V cm^{-1} in the presence of moisture and attributed it to the ion movement through electric field. Since an electric field was applied between two electrodes touching perovskite film, electric current could flow and there was a possibility of charge trapping underneath the electrode, which might have played a role for degradation. To isolate the effect of pure external electric field, we examined the degradation of perovskite materials by applying non-contact electric field which was given by two floating electrodes; one electrode is in air above perovskite film coated on ITO glass and the other electrode exists beneath the glass. We found no degradation up to 12 kV cm^{-1} under 90 % RH(See Figure 2.6). Note that this field will be dropped across the air gap and therefore, the real field inside perovskite film should be different from the given field and the perovskite film might be uniformly polarized by one-directional strong E-field because perovskite materials have a high dielectric constant.[42,43] Therefore, further study should be needed to completely understand the effect of pure external electric field. It is noted that the differences between the fields due to the trapped charges and the external field lie in the point-like character of the trapped charges, which produce locally

huge and irregular fields. The huge and irregular fields formed by charges trapped along grain boundaries could help the process of deprotonation.[20,44]

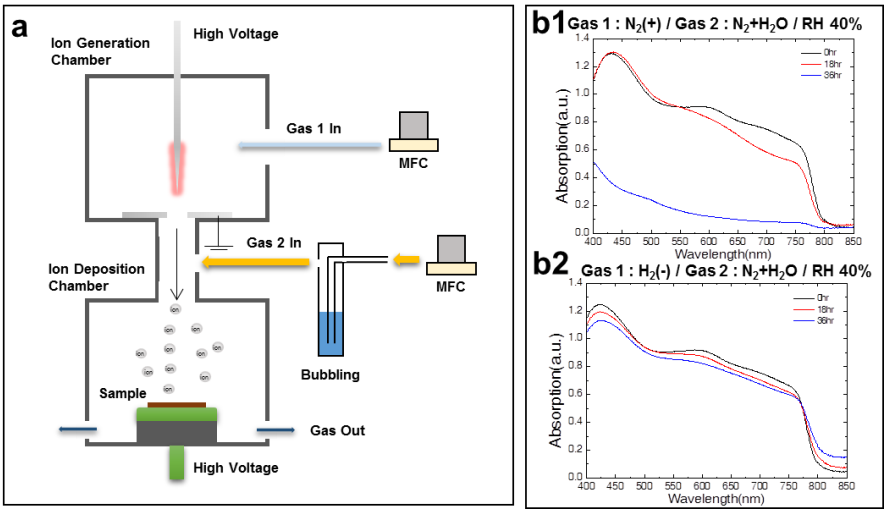

Figure 2.4 (a) Experimental setup of corona discharge for ion generation, bubbling system for humidification, and SUS chamber for ion deposition and blocking light. (b) Absorption spectra of the perovskite film measured at an interval of 18 hours during deposition of (b1) positive nitrogen ions and (b2) negative hydrogen ions at 40% relative humidity.

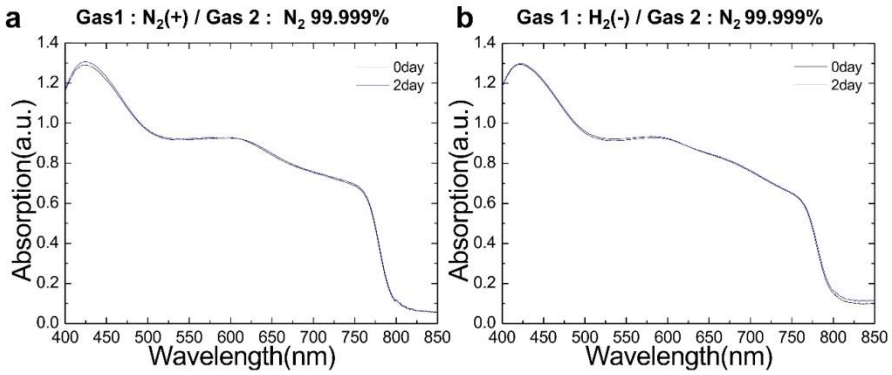

Figure 2.5 Absorption spectra of the perovskite film under (a) continuous positive nitrogen and (b) negative hydrogen ion deposition in moisture-free dark condition.

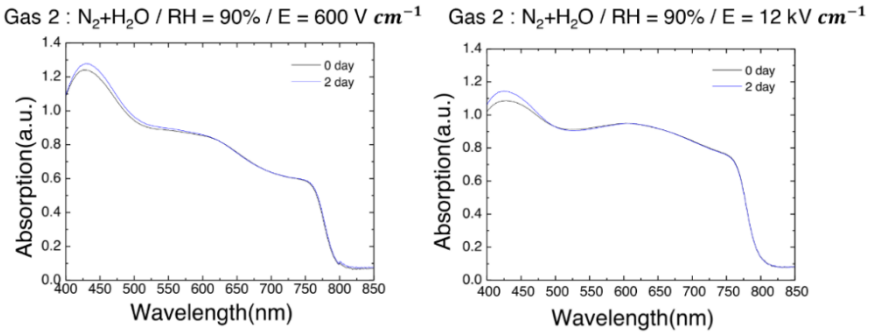

Figure 2.6 The effect of non-contact high electric field on the degradation of the perovskite film at high relative humidity (90%) under dark condition.

We also employed three experimental apparatuses for our perovskite degradation studies. Using the first apparatus that has a sealed chamber (light blocked) with a gas inlet and outlet (Figure 2.7a), we can study the reaction between a gas and perovskite film without any external perturbation. The ambient gas in the chamber was adjusted by the different combination of inlet gases. The second apparatus (Figure 2.7b) is designed for intentional charge trapping in the perovskite film without light soaking by introducing N_2^+ corona ions(Same experimental setup as mentioned above). It is noted that gas molecules such as O_2 or H_2O are mixed with N_2^+ ions in the deposition chamber after N_2^+ corona ions generated in the corona chamber are injected into the deposition chamber. N_2^+ corona ions are selectively deposited on the perovskite surface by applied electric field in the deposition chamber. In the third apparatus (Figure 2.7c), we can study the degradation of perovskite film placed in a gas-controlled chamber under solar-simulated light to investigate the synergetic effect of light soaking and gas molecules.

First, to reconfirm the effect of water molecules on $MAPbI_3$ degradation in dark condition, pure nitrogen gas was humidified through a water bubbler and injected into the sealed chamber where a $MAPbI_3$ film was placed (at the relative humidity of 40% and flow rate of 2 lpm). There was no change in the absorption spectrum of the

$MAPbI_3$ film for 24 hours as shown in Figure 2.7d, which means that water molecules alone do not cause irreversible degradation of $MAPbI_3$ perovskites in dark condition, as was reported previously[17,45]. However, Figure 2.7e and f show that either ion charge deposition (without light) or light soaking causes irreversible degradation of $MAPbI_3$ film in 24 hours under the same humidified nitrogen gas. Both ion deposition and light soaking were shown to cause charge trapping along perovskite grain boundary, where degradation was initiated, and we proposed that trapped charge would be the main cause for irreversible degradation occurred under light soaking and moisture. However, it still remains unclear how water molecules interact with $MAPbI_3$ crystal in the presence of trapped charges.

Oxygen molecules have also been suggested as a cause of irreversible degradation in previous reports.[16,24,25,46] Haque and coworkers demonstrated that $MAPbI_3$ could be decomposed by light activated oxygen (superoxide O_2^-) even without moisture.[16,24,25] In their study, a degradation test was carried out under light soaking condition in the presence of oxygen. In the present study, we were able to examine the effect of oxygen molecules on the degradation of $MAPbI_3$ with either light soaking or ion charge deposition without light.

First, we found that injection of only dry air (N_2+O_2) without charge deposition or light irradiation did not cause any degradation (Figure 2.7g). On the other hand, the $MAPbI_3$ film underwent complete degradation in 24 hours under dry air with ion charge deposition (without light) (Figure 2.7h) or under light soaking (Figure 2.7i) as was the same in the presence of moisture (Figure 2.7e, f). In light of the fact that there was no degradation in nitrogen ambient gas (Figure 2.8), oxygen molecules are believed to be responsible for chemically interacting with the compositional units of $MAPbI_3$ crystal, as will be discussed in detail later.

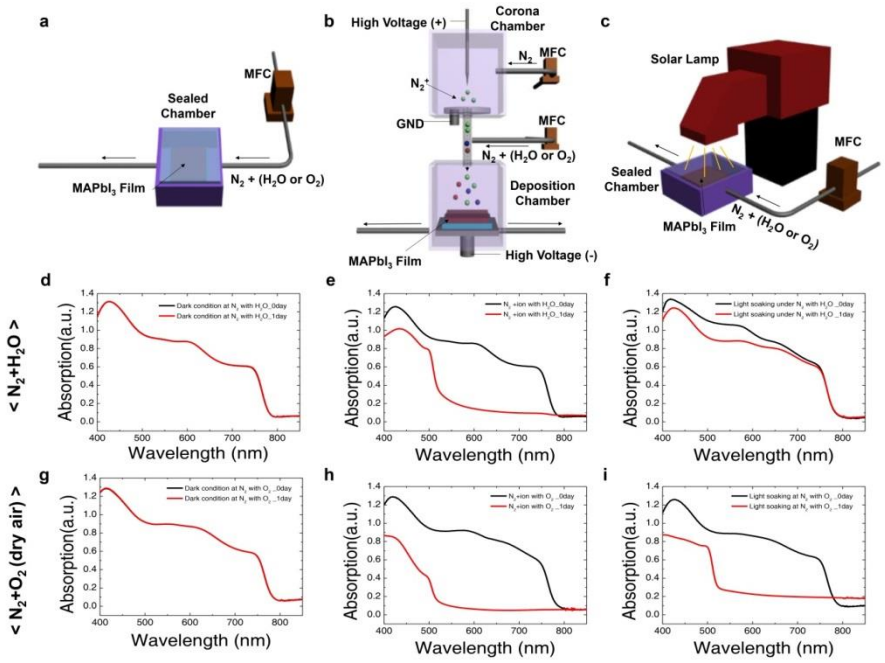

Figure 2.7 a-c, Schematic illustration of experimental apparatuses for aging test, a, under dark condition, b, with N_2^+ deposition, and c, under one-sun irradiation. d-f, Absorption spectra of $MAPbI_3$ film measured before and after 1 day of aging with a continuous flow of humidified nitrogen gas, d, under dark condition, e, with nitrogen cation deposition, and f, under one-sun irradiation. g-i, Absorption spectra of $MAPbI_3$ film measured before and after 1 day of aging with dry air, g, under dark condition, h, with nitrogen cation deposition, and i, under one-sun irradiation.

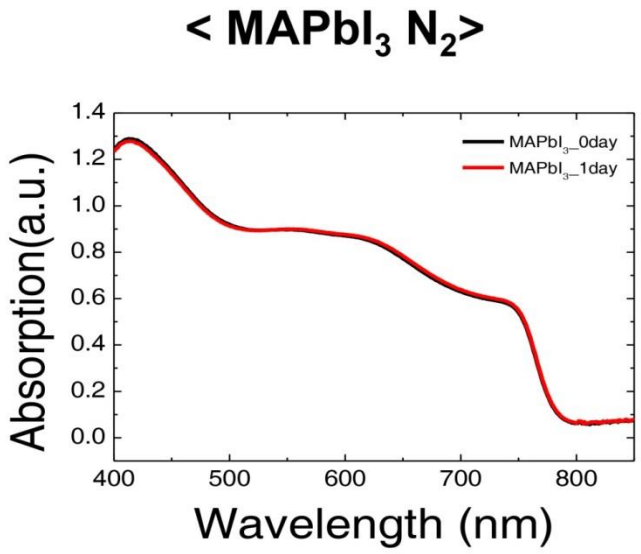

Figure 2.8 Absorption spectra of perovskite films aged under one sun irradiation in pure nitrogen ambience.

Next we investigated how trapped charge could decompose perovskite material in time by examining morphology evolution via SEM analysis. As shown in Figure 2.9a (Tilted top-view and cross-sectional images) and Figure 2.10 (Top-view images), the degradation is initiated from the grain boundaries. As the reaction continues, the color of the film turns into yellow, indicating that the perovskite is irreversibly decomposed to PbI_2. It is interesting to dig into why degradation occurs from grain boundaries in line with our trapped charge mechanism. To check the distribution of trapped charges on the surface of perovskite after uniform ion deposition, we measured Kelvin Probe Force Microscopy (KPFM) of un-treated perovskite and ion-treated perovskite films (see more details in Experimental methods: Topography and Kelvin probe force microscopy). Figure 2.9b shows topology and surface potential distribution of the perovskite surface on which positive N_2 ions were uniformly showered. Striking coincidence between two images is the evidence that charges are preferentially trapped along grain boundaries. Overlapped image of topology and potential distribution shown in Figure 2.11 clearly demonstrates charges are trapped along grain boundaries even though ions are showered uniformly. For untreated sample, there is no correlation between topology and potential distribution (see Figure 2.11). With this charge trapping

along grain boundaries, experimentally observed degradation pattern following grain boundaries and the fact that the irreversible degradation occurs only when moisture or oxygen and charges exist together are the evidences that trapped charges would be responsible for the initiation of irreversible degradation of perovskite materials. It is now apparent that grain boundaries are the most vulnerable sites for the degradation because they provide charge accumulation sites as well as infiltration pathway of water vapor or oxygen.[19,25] Successful enhancement of stability utilizing high mobility inorganic charge extraction layers supports the present idea.[11,27]

To further investigate the possibility that the above mentioned intriguing experimental observation of irreversible degradation under light soaking might be related to the mechanism of trapped charges of the present study, we measured KPFM images on the surface of perovskite after light illumination without ion deposition. As shown in Figure 2.11, charges are clearly trapped along grain boundaries for the sample soaked by light confirming that light soaking alone induces charge trapping along the grain boundaries of perovskite material like was done by introduction of ion charges in the dark condition. From our concept, these trapped charges can now trigger the irreversible degradation due to moisture or oxygen as the same happened when ion charges are deposited in the dark. Therefore, the

fundamental cause for irreversible degradation would be the same, that is, the trapped charges that could trigger the irreversible degradation under humid air. Such irreversible degradation under light soaking was reported in previous several reports[30,34], but, the reason has not been clearly elucidated so far although Christians et al.[30] suggested the lessened hydrogen bonding after photoexcitation as a possible cause. Here, we argue that trapped charges under moisture or oxygen would be responsible for the initiation of irreversible degradation under light or in the dark since light illumination always generates charges and traps the charges along grain boundaries as shown earlier. This can explain well why moisture itself without illumination or intentional ion deposition only hydrated perovskite reversibly. Light illumination under nitrogen gas without moisture and oxygen for one day was shown to hardly degrade the perovskite as shown in Figure2.8 which is strongly contrasted with the case of light illumination under humid air (see Figure 2.3b).

We also investigated charge trapping details through high resolution KPFM measurements (Figure 2.12). High-resolution KPFM images of the fresh samples under light soaking or with nitrogen ion deposition clearly show that the location of trapped charges is dominantly along grain boundaries and on some spots of

grain surfaces. We also found that oxygen-induced degradation took place along the grain boundaries and on grain surfaces where charges are mainly trapped, as shown by high-resolution KPFM and Field Emission-Scanning Electron Microscopy (FE-SEM) images of the fresh and degraded samples (Figure 2.13). Moreover, the evolution of surface potential distribution was observed during the whole degradation process, it was confirmed that charges continuously trapped along the grain boundaries (Figure 2.14). Since the morphology and area of the degraded sample changed with time, root mean squared roughness values of potential distributions increased during the degradation, which is indicative of occurring more widespread degradation with time (Figures 2.13 and 2.14). Thus, we may hypothesize that trapped charges along grain boundaries trigger irreversible degradation of $MAPbI_3$ perovskites in the presence of water or oxygen.

In addition, Photoluminescence(PL) spectroscopy measurements were performed to investigate charge trapping when positive N_2 ion deposited(Figure 2.15). In steady-state PL measurements, the detected PL intensity of $MAPbI_3$ film was decreased after positive N_2 ion deposition. In time-resolved PL(TRPL) measurements, the slope of PL decays was steeper after positive N_2 ion deposition. It is also confirmed that the first time constant(τ_1) achieved from TRPL by the

3-exponential fitting decreases from 45ns to 6.9ns after positive N_2 ion deposition.(Table 2.1) These results are similar to those obtained when measuring perovskite films with charge extraction layers.[47] In the case of PL measurements of the perovskite film with charge extraction layer, the charges generated by the light are extracted to the charge extraction layer, so the recombination of excitons is reduced. As the result, the PL intensity in steady-stat PL and first time constant in TRPL are decreased. Therefore, from the above results, it can be expected that the positive nitrogen ion deposited by the corona discharge method stays on the perovskite layer and acts as a trapped charges.

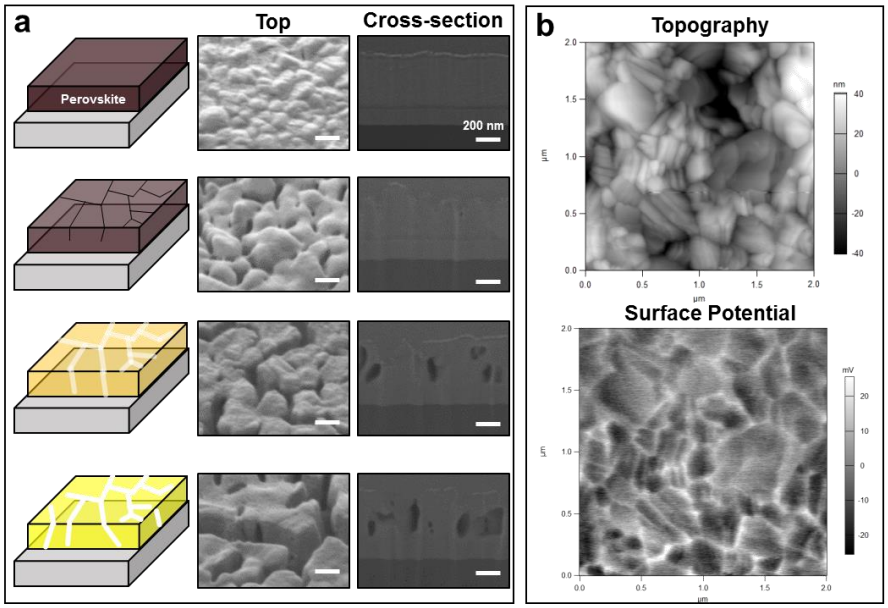

Figure 2.9 (a) Scheme description of perovskite degradation processes (left), and top-view (middle) and cross-sectional (right) SEM images of perovskite layers by ion deposition in humidified nitrogen. Scale bars = 200 nm. (b) Topography and surface potential profile of the perovskite film obtained from KPFM measurements after deposition of N_2 positive ions.

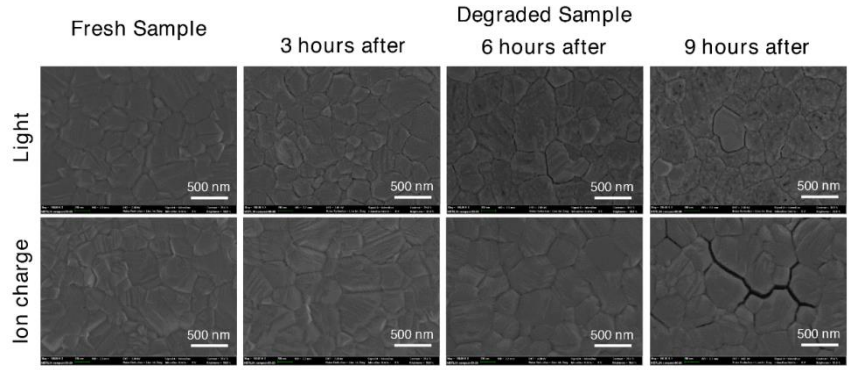

Figure 2.10 The top-view SEM images of the fresh and degraded perovskite films. The degraded samples were aged for 9 hours under one sun light illumination (first row) and ion charge deposition (second row), respectively.

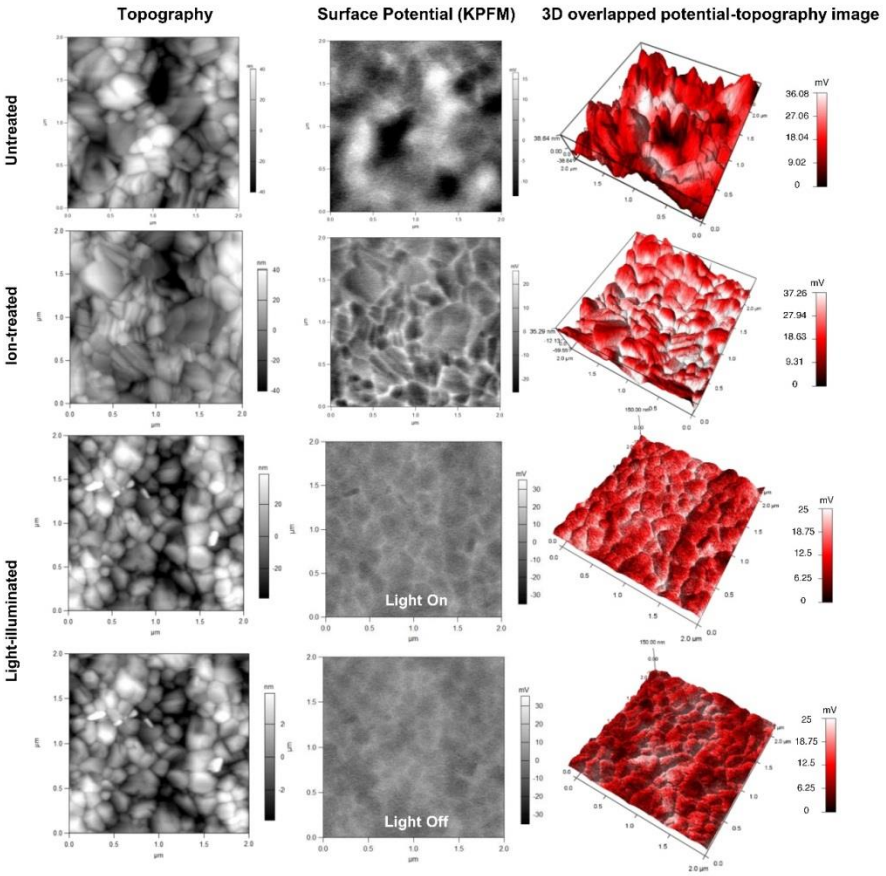

Figure 2.11 Topographies (first column) and surface charge density profiles (second column) of untreated (first row), Ion-treated (second row), and light-illuminated (third and fourth row) the perovskite film. The images in the third and fourth row were obtained from light on and off during the measurement, respectively. The images in the third column show 3D plots of topographies colored based on the surface potential values. Both images of light illuminated cases show clear charge trapping

along grain boundaries, but the charge trap is more contrasted when KPFM operation is under the light on

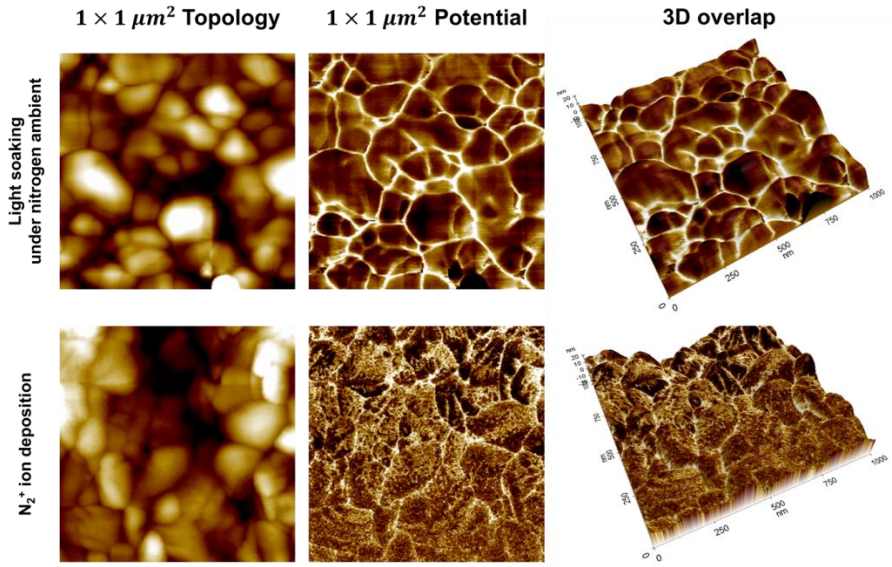

Figure 2.12 High-resolution KPFM images of $MAPbI_3$ film after light soaking and nitrogen cation deposition

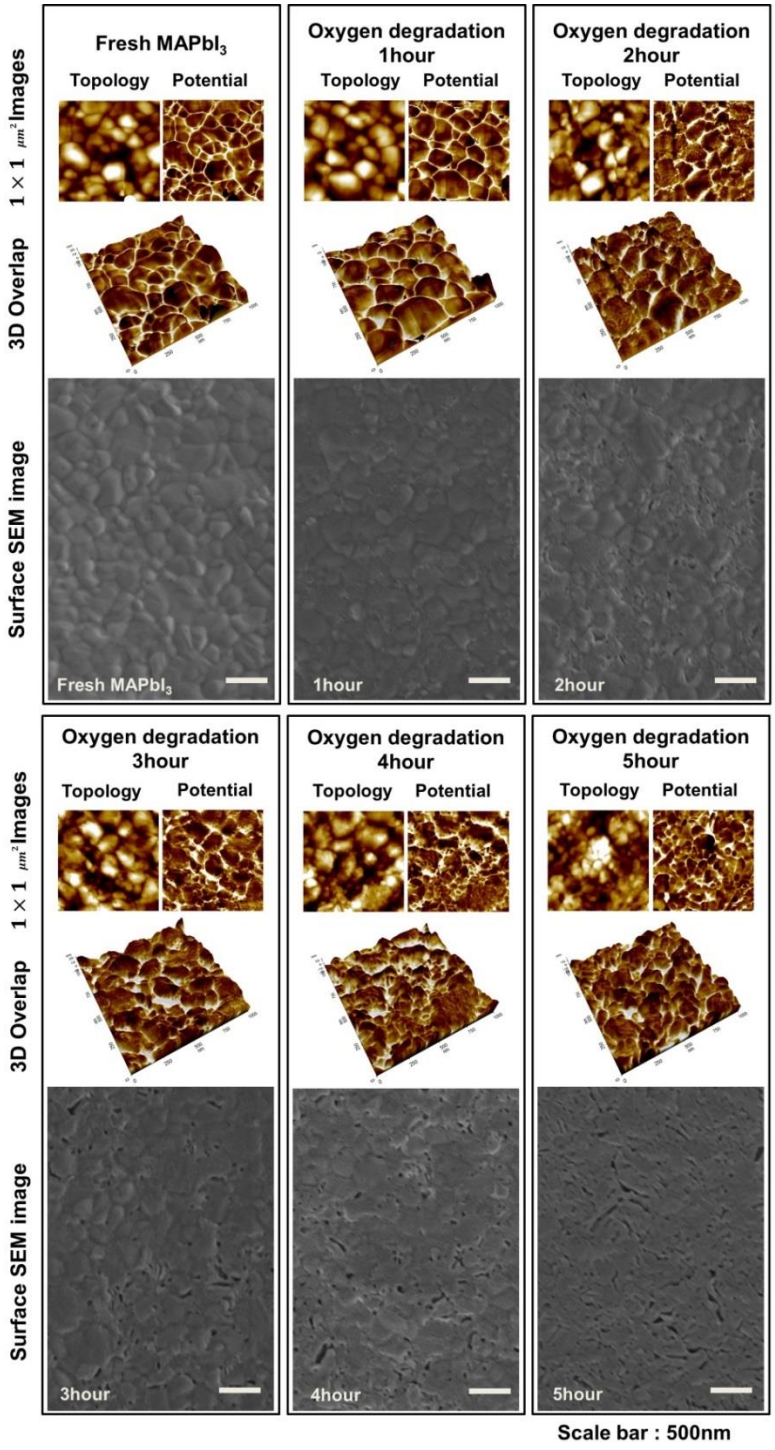
Fresh MAPbI3
Topology
Potential
Oxygen degradation 1hour
Topology
Potential
Oxygen degradation 2hour
Topology
Potential
1 × 1 μm² Images
3D Overlap
Surface SEM image
Fresh MAPbI3
1hour
2hour
Oxygen degradation 3hour
Topology
Potential
Oxygen degradation 4hour
Topology
Potential
Oxygen degradation 5hour
Topology
Potential
1 × 1 μm² Images
3D Overlap
Surface SEM image
3hour
4hour
5hour
Scale bar : 500nm

Figure 2.13 Time evolution of high-resolution KPFM images and top-view SEM images for the $MAPbI_3$ film. The $MAPbI_3$ films coated on the C_{60}(35nm)/ITO substrate were degraded under one sun light illumination in 100% oxygen ambient.

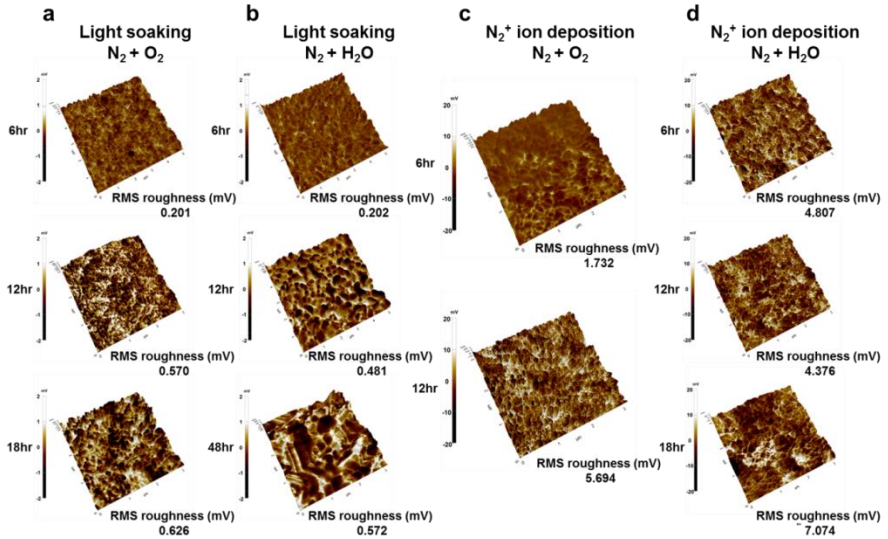

Figure 2.14 Time evolution of KPFM images of $MAPbI_3$ films degraded under difference charge generation condition in humidified nitrogen or dry air. (RMS roughness is defined by $\text{RMS roughness} = \sqrt{\frac{1}{N}\sum_{i=1}^{N} V_i^2}$ **where V_i is a potential difference of pixel i and N is the total number of pixels of the measured area)**

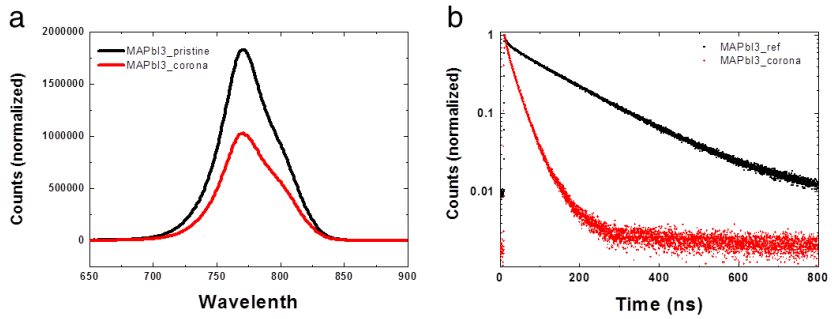

Figure 2.15 (a) Normal PL and (b) Time resolved PL measurements of $MAPbI_3$ film before and after positive N_2 ion deposition

Unit (s)	τ_1	τ_2	τ_1
MAPbI3_Ref	4.49E-08	1.67E-07	5.71E-09
MAPbI3_corona	6.89E-09	2.75E-08	7.09E-08

Table 2.1 Time constant of $MAPbI_3$ film from Time resolved PL by 3-exponentials fitting.

Although the easy degradation of hybrid perovskite is a widely known problem, there is no clear theory to date that explains its mechanism from the atomic-scale viewpoint. However, we can readily apply a computational method to simulate how $MAPbI_3$ grain surfaces (including grain boundaries) evolve via our hypothesis on trapped-charge driven degradation. In this study, we first carried out AIMD simulations on the basis of density functional theory (DFT) calculations to examine molecular interaction of gaseous molecules (O_2 and H_2O) and the evolution of the $MAPbI_3$ grain surface in the presence of charge trapping. In all simulations, we adopted an initial geometry with 2 rigidly fixed $MAPbI_3$ units in the bottom of the crystal, 2 structurally relaxed $MAPbI_3$ units on top of the 2 bottom units to form the surface, and adsorbate molecules on the surface. We bestowed different net charge (+1, 0, or −1) in the unit cell to simulate the trapped charge resulting from the separation of excitons generated by light.

We first carried out simulations for the pure $MAPbI_3$ surface without any adsorbate as a control case, which resulted in no special outcome regardless of the net charge trapped (Figure 2.16). This means that trapped charges themselves do not cause any degradation if there are no gas molecules. To investigate the effect of water molecules in the presence of trapped charge, we performed

simulations for five water molecules randomly placed near the surface (Figure 2.17). In the neutral case with no trapped charge (Fig. 2.17b), all water molecules evolved out of the $MAPbI_3$ surface and clustered with themselves in 2 ps although some of them were quite solidly embedded initially. However, when an electrostatic charge was injected to the crystal, notable changes occurred in atomic motions. In the positively charged crystal (Figure 2.17c), the five water molecules quite evenly placed initially on the $MAPbI_3$ surface started to cluster around a methylammonium cation ($CH_3NH_3^+$). The $CH_3NH_3^+$ cation ended up effectively solvated by water molecules through hydrogen bonds ($N\text{-}H\cdots OH_2$), indicating the dissolution of $CH_3NH_3^+$ cations into the surface water on the bulk solid with trapped positive charges. The distance between hydrogen of CH3NH3+ and oxygen of water during the simulation (Figure 2.18d) obviously shows the existence of hydrogen bonds from which the strong $CH_3NH_3^+$-H_2O interaction is inferred. Such a dissolution process appears prompted by the weakened bond between $CH_3NH_3^+$ cation and the PbI_6^- octahedron unit due to the new electrostatic force field induced by the excess positive charge. In the negatively charged crystal (Figure 2.17), on the other hand, a totally different water-induced degradation pathway was discovered. In contrast to the positively charged crystal, water molecules now aggregate

around an iodide anion (I^-) that is fast moving away from its stable position on the surface due to the electrostatic expulsion by the excess negative charge. The elevated height of I^- during the negatively charged simulation compared to the neutral or positively charged cases (Figure 2.18e) clearly shows the dissociation of I^- from the perovskite surface. A subsequent encounter between this hydrated I^- anion with water molecules would result in volatile species such as hydrogen iodide (HI) and methylamine (CH_3NH_2), as shown in the 2 ps snapshot of Figure 2.17, from proton transfer between $CH_3NH_3^+$ and I^-. The calculated bond length of HI at 2 ps in Figure 2.17 is 1.616 Å, which is very similar to the known value of 1.609 Å. It is noted that the generation of these volatile compounds in the presence of water molecules is predicted for the first time by simulation although the release of such volatile compounds from the perovskite solid has been previously suggested[20,44,48]. The deprotonation of organic cation initiated by trapped charge consists of the following three steps as shown in Figure 2.19.

$I^- + H_2O \rightarrow HI + OH^-$ (shown at 1.75 ps of Figure 2.19)

$OH^- + H_2O \rightarrow H_2O + OH^-$ (shown at 1.80 ps and 1.85 ps of Figure 2.19)

$CH_3NH_3^+ + OH^- \rightarrow CH_3NH_2 + H_2O$ (shown at 1.90 ps and 1.95 ps

of Figure 2.19)

The overall reaction is seen to initiate from proton transfer from one of the surrounding water molecules to an iodide anion (1.75 ps in Figure 2.19), which is followed by sequential water-to-water proton exchange until it eventually ends up in proton transfer from $CH_3NH_3^+$ to OH^- (1.80 ps ~ 1.95 ps in Figure 2.19). Such a sequential proton transfer pathway akin to the Grotthuss mechanism through a series of hydrogen bonds may very well be energetically favorable over direct proton transfer from $CH_3NH_3^+$ to I^- due to the stabilization of intermediate and transition states. Our AIMD simulation clearly demonstrates the crucial role of water in the degradation of $MAPbI_3$ crystal in the presence of trapped charges as it enables both the solvation of component ionic species and the sequential proton transfer. To check the effect of unit cell size, we performed additional simulations using 2 × 1 supercell with same charge density (Figure 2.20), and to confirm the effect of time-step and simulation time, we also carried out simulations over 4 ps using 1.5 fs time-step with original unit cell (Figure 2.21). For both kinds of simulations, almost the same events were observed including the solvation of $CH_3NH_3^+$ cations with strong hydrogen bonds in positively charged case (Figure 2.20d and Figure 2.21d) and the

encircling of dissociated I^- anion (Figure 2.20e and Figure 2.21e) and $CH_3NH_3^+$ cation by water molecules to make a proton transfer reaction in negatively charge case. In addition, the charge sum of 5 H_2O molecules at the initial geometry (Figure 2.17a) is –0.13, –0.23, and –0.47, and the charge on MAPbI3 surface is +1.13, 0.23, and –0.53 for positively, neutrally, and negatively charged unit cell respectively, which means that the most of injected charge (+0.90 of +1.00 and –0.76 of –1.00) is delocalized on $MAPbI_3$ at first.

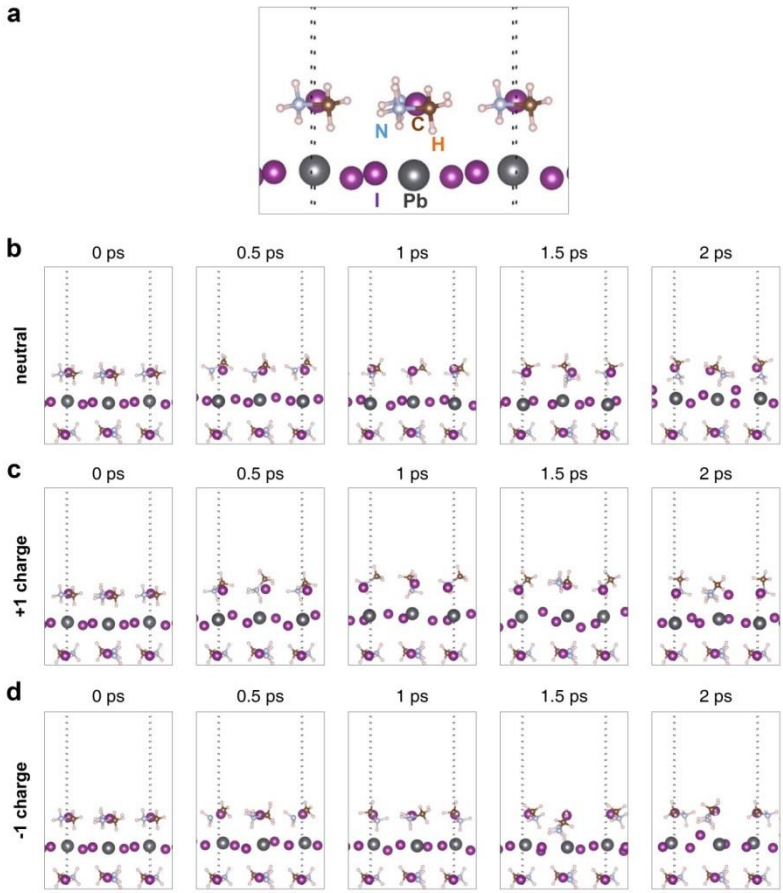

Figure 2.16 a, Expanded view for the initial geometry of pure $MAPbI_3$ surface. b-d, Temporal snapshots of the AIMD simulated atomic trajectories of $MAPbI_3$ crystal with a charge of b, 0, c, +1, and d, −1. All simulations start with the same initial geometry at 0 ps shown in a. Dotted vertical lines represent the boundaries of actual simulation space, beyond which repeated images of atoms are shown because of the periodic boundary condition.

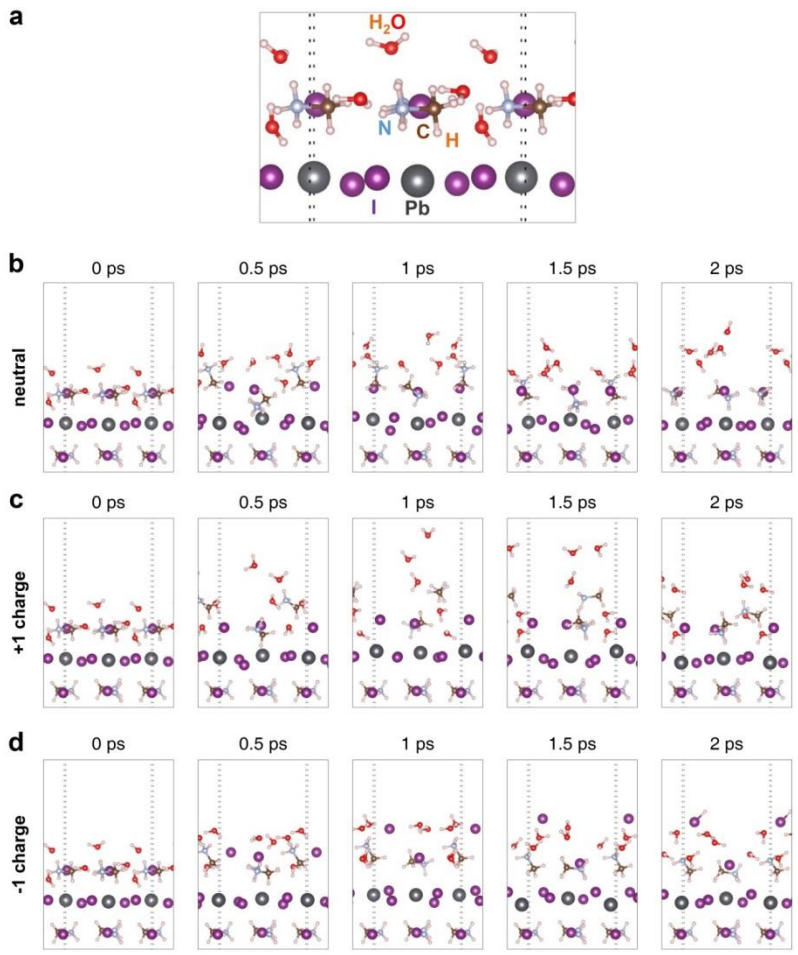

Figure 2.17 a, Expanded view for the initial geometry of 5 H_2O molecules on the $MAPbI_3$ surface. b-d, Temporal snapshots of the AIMD simulated atomic trajectories of $MAPbI_3$ crystal with a charge of b, 0, c, +1, and d, −1. All simulations start with the same initial geometry at 0 ps shown in a. Dotted vertical lines represent the boundaries of actual simulation space, beyond which repeated images of atoms are shown because of the periodic boundary condition.

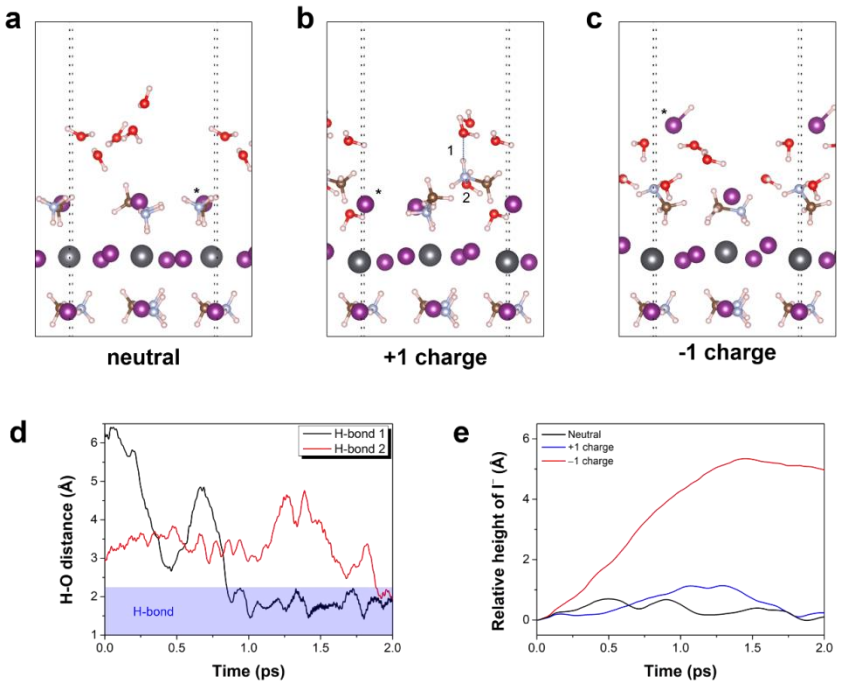

Figure 2.18 a-c, Snapshots at the 2 ps of the AIMD simulations in Fig. 2.17 with a charge of a, 0, b, +1, and c, −1. d, The distances between hydrogen and oxygen atom shown as navy dotted line in b during the positively charged simulation. e, The relative height of asterisk marked I^- in a, b, and c compared to the initial position during each simulation.

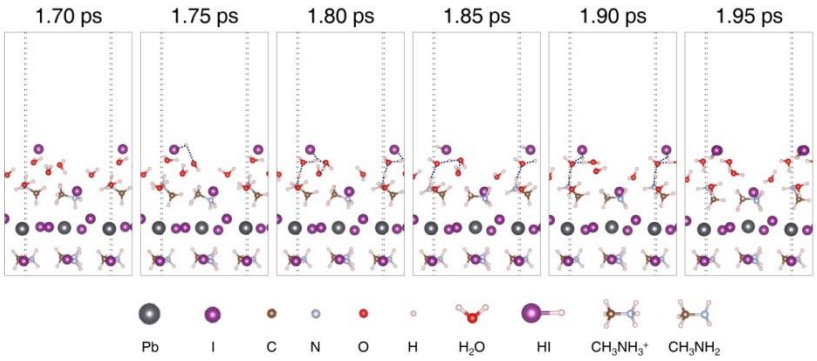

Figure 2.19 Temporal snapshots of the AIMD simulated atomic trajectories of $5H_2O$-covered $MAPbI_3$ crystal with a charge of −1 during the proton transfer. Hydrogen bonds in proximity that form proton wires are shown by navy dotted lines. Dotted vertical lines represent the boundaries of actual simulation space, beyond which repeated images of atoms are shown because of the periodic boundary condition.

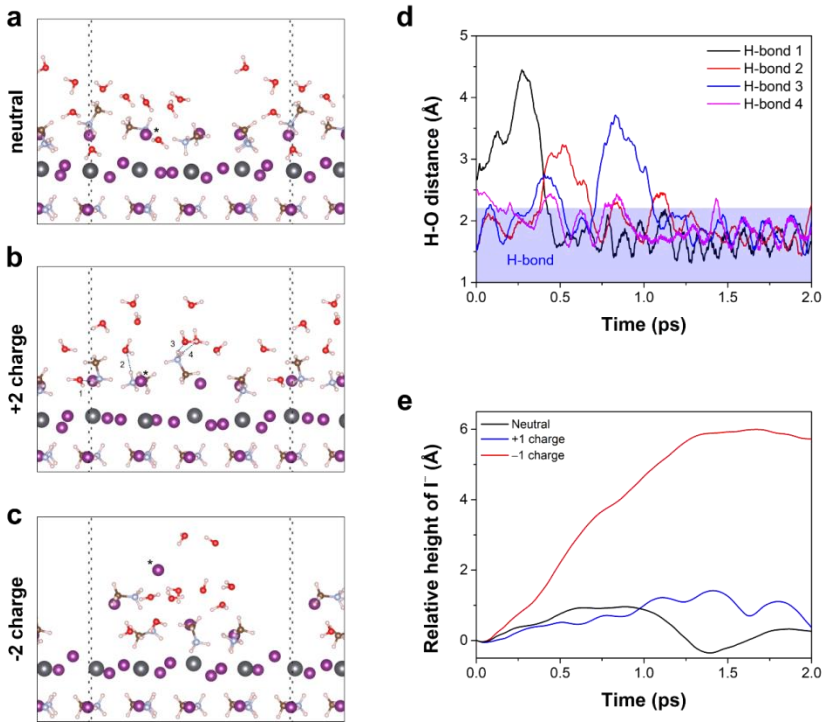

Figure 2.20 a-c, Snapshots at the 2 ps of the AIMD simulations with a charge of a, 0, b, +2, and c, −2 whose initial geometries are 2 × 1 supercell of Fig. 2.17a. d, The distances between hydrogen and oxygen atom shown as navy dotted line in b during the positively charged simulation. e, The relative height of asterisk marked I^- in a, b, and c compared to the initial position during each simulation.

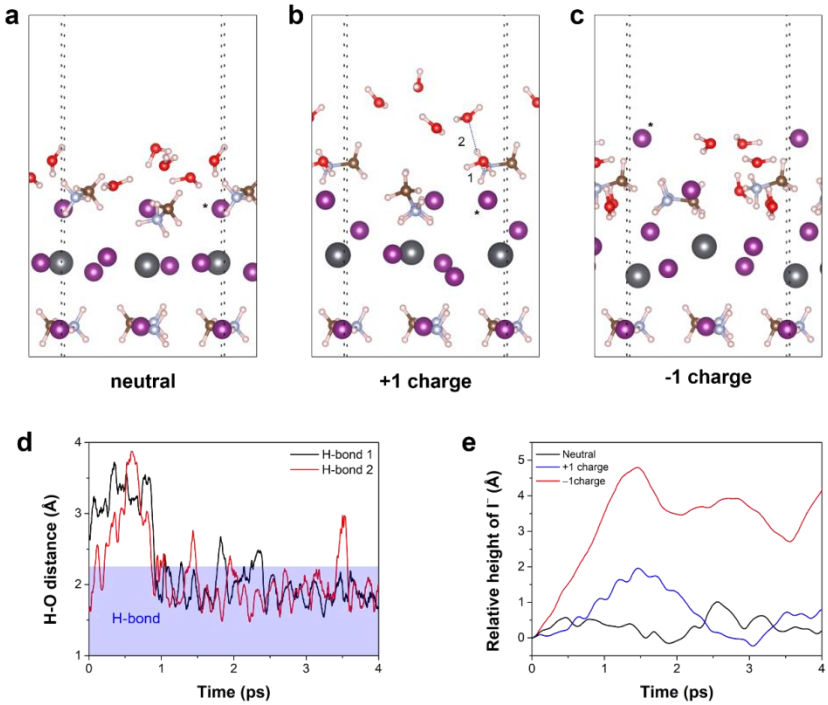

Figure 2.21 a-c, Snapshots at the 4 ps of AIMD simulations with a charge of a, 0, b, +1, and c, −1 using 1.5 fs time-step whose initial geometries are same as Fig. 2a. d, The distances between hydrogen and oxygen atom shown as navy dotted line in b during the positively charged simulation. e, The relative height of asterisk marked I^- in a, b, and c compared to the initial position during each simulation

We also investigated the effect of oxygen as it is newly shown to cause complete, rapid degradation of $MAPbI_3$ film following charge deposition (Figure 2.7h) or light soaking (Figure 2.7i). Although Haque and coworkers[24,25] assumed that defect sites of $MAPbI_3$ crystals provide a trap site for oxygen molecules on their way to superoxide formation, we considered no defect sites in our simulation and examined only surface degradation pathways involving oxygen in the presence of trapped charges. As a test case, we first simulated a $MAPbI_3$ surface with four embedded nitrogen molecules with or without trapped charges (Figure 2.22). All embedded nitrogen molecules escaped from the surface and flew away within 2 ps regardless of the net charge, which indicates that nitrogen molecules are not involved in any significant interaction with the constituents of $MAPbI_3$ perovskite, as can be easily expected. We then carried out simulations for oxygen molecules with the same geometry as the nitrogen molecules in our test run. In stark contrast to the nitrogen case, most of oxygen molecules persisted near the surface regardless of the net charge (Figures 2.23b, 2.23c, and 2.23d), which suggests that oxygen is involved in strong chemical interaction with the component species of $MAPbI_3$. Additionally, we observed the formation of oxides in positively (+1) (Figure 2.23c) and negatively (−1) (Figure 2.23d) charged case but

not in the neutral case (Figure 2.23b). Superoxide species were also observed in the presence of a charge, which is in good agreement with previous studies.[25](See Table 2.2) We had a glimpse of a transient interaction toward oxide formation in the middle of simulation (0.5 ps ~ 1.5 ps in Figure 2.23b), but it did not lead to actual bond formation between oxygen and I^- anion or Pb^+ cation in the absence of charge. On the other hand, in positively or negatively charged perovskite crystal (Figures. 2.23c and 2.23d), the strong interaction of oxygen with the compositional species of $MAPbI_3$ resulted in the formation of stable I–O or Pb–O bonds.

To confirm the generation of oxides, we additionally analyzed the I–O, Pb–O, and O–O distances for atoms of interest (those forming the I–O–O–Pb bond at 0.5 ps of Figure 2.23b and 1 ps of Figures. 2.23c and 2.23d) throughout the simulation. In the absence of any charge, the I–O and Pb–O distances are quite short (~2.1 Å and ~2.5 Å, respectively) in the early stage of simulation (0 ~ 1 ps) but become longer past 1 ps (Figures. 2.23e and 2.23f), whereas the O–O distance, to the contrary, start out as a long bond (~1.4 Å) but becomes shorter past 1 ps (Figure 2.23g). These observations mean that oxygen do not form stable bonds with the neighboring Pb or I atoms without charge. On the contrary, in the presence of trapped charge, the I–O, Pb–O, and O–O distances show continued

vibrational oscillation, indicating the existence of permanent chemical bonds (Figures. 2.23e, 2.23f, and 2.23g). To determine the superoxide character of the oxygen atoms in question, we carried out Bader population analysis for the 2-ps geometry with a charge of +1, 0, and −1, and confirmed that only oxygen molecules that are bonded to perovskite (oxygen 1 for +1 charged simulation and oxygen 1 and 2 for −1 charged simulation shown in Figure 2.23) have almost −1 charge (Table 2.2). We additionally examined the vibrational frequencies (or periods) of O–O shown in Figure 2.23g in order to verify the formation of oxides. The vibrational period of the O–O bond with no charge is 24.3(±1.0) fs (at 1 ~ 1.5 ps), which is comparable to the experimental value of 21.4 fs (1,556 cm^{-1}) corresponding to free gaseous oxygen molecule[49], but it becomes much longer (41.1(±8.8) and 39.7(±6.7) fs, respectively) in positively and negatively charged crystal. These longer vibrational periods or lower vibrational frequencies are indicative of a weaker O–O bond and simultaneously stronger I–O and Pb–O bonds in the presence of charge, which should be associated with trapped-charge driven oxidation. Also, the charge sum of 4 O_2 molecules at the initial geometry (Figure 2.23a) was –1.47, –1.65, and –2.07, and the charge on $MAPbI_3$ surface is +2.47, +1.65, and +1.07 for positively, neutrally, and negatively charged unit cell respectively, which

implies that the most of injected charge (+0.82 of +1.00 and –0.58 of –1.00) is delocalized on $MAPbI_3$ at first like the preceding water cases. Although quite large portion of injected charge (–0.42) is delocalized on O_2 molecules, it is natural electron transfer process to form a superoxide (O_2^-) because of the electrophilic property of oxygen.

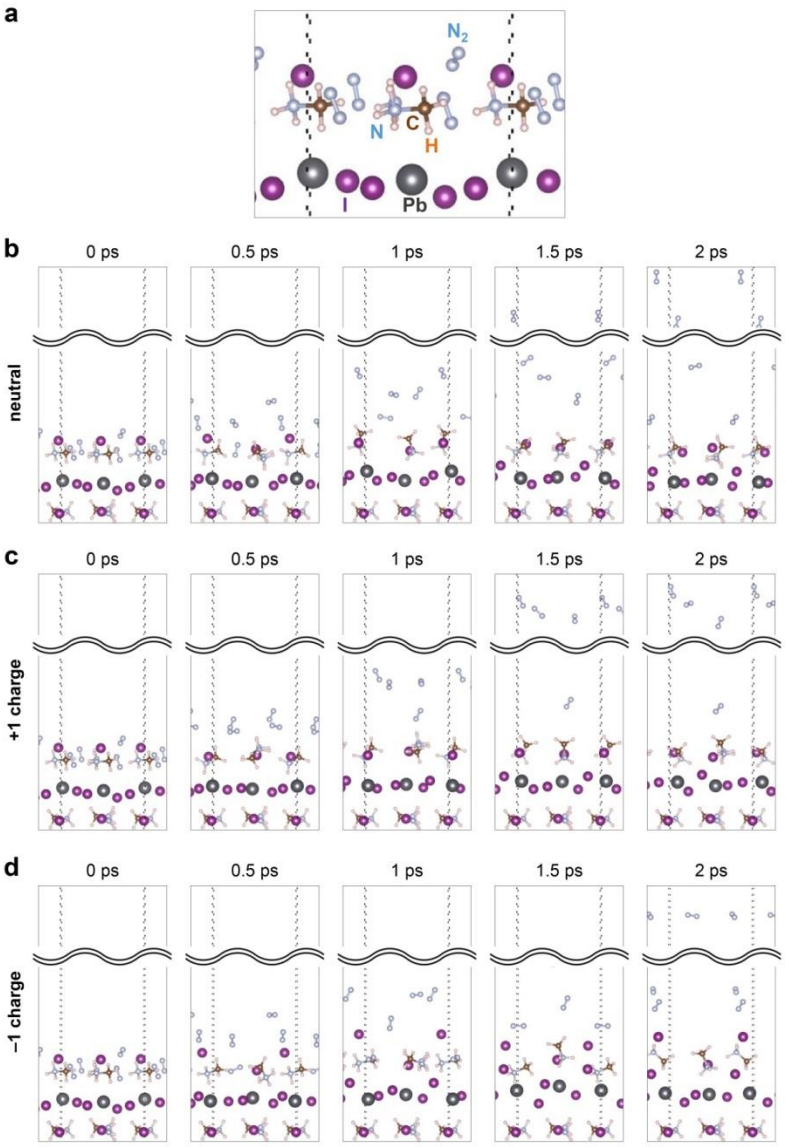

Figure 2.22 a, Expanded view for the initial geometry of $4N_2$-covered $MAPbI_3$ surface. b-d, Temporal snapshots of the AIMD simulated atomic trajectories of $4N_2$-covered $MAPbI_3$ crystal with a charge of b, 0, c, +1, and d, −1. All simulations start with

the same initial geometry at 0 ps shown in a. Dotted vertical lines represent the boundaries of actual simulation space, beyond which repeated images of atoms are shown because of the periodic boundary condition.

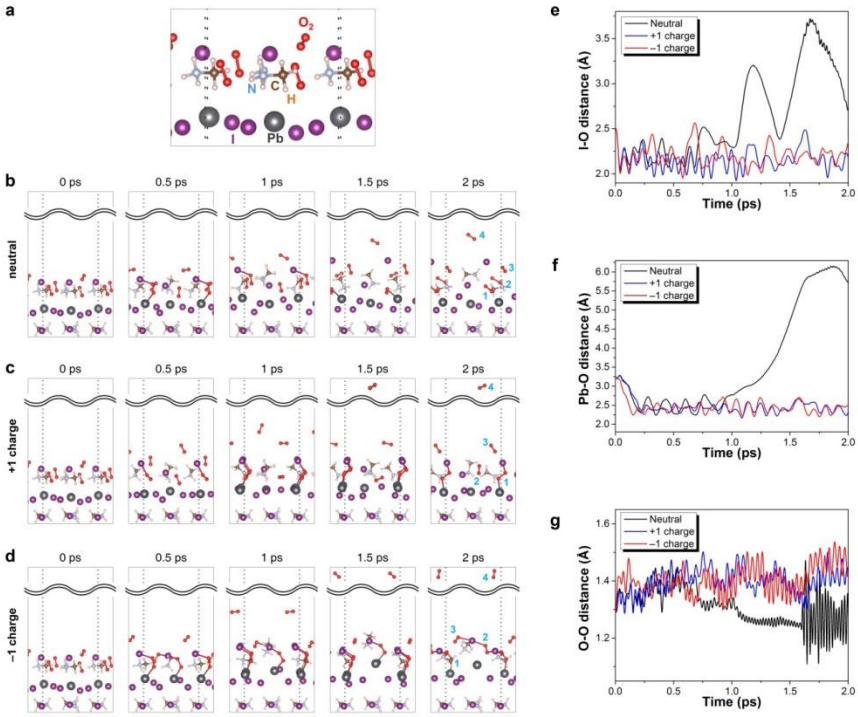

Figure 2.23 a, Expanded view for the initial geometry of 4 O_2 molecules on the $MAPbI_3$ surface. b-d, Temporal snapshots of the AIMD simulated atomic trajectories of $MAPbI_3$ crystal with a charge of b, 0, c, +1, and d, −1. All simulations start with the same initial geometry at 0 ps shown in a. Dotted vertical lines represent the boundaries of actual simulation space, beyond which repeated images of atoms are shown because of the periodic boundary condition. In the 2-ps snapshots, oxygen molecules are designated by numbers for charge analysis (Table 2.2). e-g, Temporal change in the e, I–O, f, Pb–O, and g, O–O distance in the I–O–O–Pb bond.

Net charge		Oxygen			
		1	2	3	4
0	status	nonbonded	nonbonded	nonbonded	nonbonded
	charge	−0.42	−0.38	−0.19	−0.02
+1	status	bonded	nonbonded	nonbonded	nonbonded
	charge	−0.94	−0.08	+0.01	+0.19
−1	status	bonded	bonded	nonbonded	nonbonded
	charge	−1.04	−0.98	−0.55	−0.13

Table 2.2. Character of chemical interaction with perovskite (top entry) and electrostatic charge (bottom entry in number) of 4 oxygen molecules with the geometry at 2 ps snapshot for $4O_2$-covered $MAPbI_3$ shown in Figure 2.23.

2.3. Conclusions

We found that trapped charges would be responsible for triggering the irreversible degradation in the moisture or oxygen induced degradation of perovskite materials. To verify this, we designed a novel experimental setup enabling the deposition of charges on the surface of perovskites for controlled moisture or oxygen degradation experiments. From this setup, we demonstrated that the perovskite materials degraded irreversibly along grain boundaries only when both moisture or oxygen and trapped charge exist simultaneously. Our study explains both why the degradation begins to occur from the different side of interface between perovskite and charge extraction layer for different charge extraction layers and how light soaking always degrades irreversibly in the presence of moisture or oxygen. KPFM study reveals that charges are trapped preferentially along grain boundaries of perovskites even under uniform deposition of ion charges or uniform illumination of light, which supports our idea of trapped charge driven degradation.

We also investigated interactions between gas molecules and $MAPbI_3$ crystal in the first 2 ps of perovskite degradation by tracking atomic motions using AIMD simulation. We found that different polarities of trapped charge lead to atomically different routes of degradation. In particular, in the negatively charged crystal, our

calculation for water-covered perovskite clearly showed that the deprotonation of $CH_3NH_3^+$ that has so far been only hypothesized in several previous studies can actually occur in water-mediated pathways. On the other hand, in our simulations for oxygen-covered perovskite, we found that trapped charge weakens the Pb–I bond and leads to stronger I–O and Pb–O interactions.

2.4. Experimental methods

Solar cell fabrication

Indium tin oxide-coated (ITO) glass substrates (AMG, 9.5Ω cm^{-2}, 25×25 mm^2) were sequentially sonicated in acetone, isopropanol, and deionized water. The cleaned substrate was sufficiently dried in oven in order to eliminate all residual solvents. A 35nm thick C_{60} layer[21] was densely coated on the ITO glass substrates by using a vacuum thermal evaporator at the constant rate of 0.1Å s^{-1}. For the $MAPbI_3$ solution, equimolar amounts of metyhlammoium iodide (MAI), PbI_2, and dimethylsulfoxide (DMSO) (i.e., 159 mg of MAI (Xi'an Polymer Light Technology), 461 mg of PbI_2 (Alfa Aesar), and 78 mg of DMSO (Sigma-Aldrich)) were dissolved in 0.6 ml of dimethylformamide (DMF) (Sigma-Aldrich). After spin coating at 4000 rpm for 20s with ether dripping treatment, the transparent adduct films were sequentially annealed at 65 ^oC for 1 min and 100 ^oC for 4 min to form black perovskite films. To prepare the hole trasport material(HTM), 72.3mg of Spiro-MeOTAD(Merk) dissolved in 1mL Chlorobenzen(Sigma-Aldrich) with 28.8 μl of 4-tert-butyl pyridine and 17.5 μl of lithium bis (trifluoromethanesulfonyl) imide (Li-TFSI) solution (520 mg Li-TSFI in 1 ml acetonitrile (Sigma–Aldrich, 99.8%)). The HTM solutions were spin-coated onto the perovskite layer at 2000rpm for 30s. After all process, 50nm gold

(Au) as a counter electrode was deposited on the HTM at the rate of 0.3 Å s^{-1} by using a vacuum thermal evaporator.

In the case of TiO_2-based devices, a TiO_2 blocking layer was fabricated on FTO-coated glass substrates by spin-coating 0.15 M titanium di-isopropoxide dis(acetylacetonate) (Sigma-Aldrich, 75 wt% in isopropanol) in 1-butanol (Sigma-Aldrich, 99.8%) at sequentially increasing spin rate of 700 rpm for 8 s, 1000 rpm for 10 s and 2000 rpm for 40 s. After spin-coating, the TiO_2 blocking layer was heated at 125 ^{o}C for 5 min, and this process was repeated once again. The substrate was annealed at 550 ^{o}C for 1 hr. The rest of the processes are identical to the fabrication of C_{60}-based devices.

Characterization

The cross-sectional and surface images of the perovskite films and the fabricated perovskite solar cells were obtained from a high-resolution scanning electron microscope with a focused ion beam system (Carl Zeiss, AURIGA). The optical absorption spectra of the perovskite films coated on the ITO substrate were measured by UV-vis spectrophotometer (Agilent Technologies, Cary 5000) in the 400-850 nm wavelength range. The XRD patterns of the perovskite films on the ITO glass were collected by using New D8 Advanced (Bruker) in the 2θ range of 5-80 degrees. Photocurrent density-voltage curves were measured by a solar simulator (Oriel Sol3A) with keithley 2400

source meter under AM1.5G, which is calibrated to give 100 mW cm^{-2} using a standard Si photovoltaic cell (Rc-1000-TC-KG5-N, VLSI Standards). The J-V curves were measured by covering devices with a metal mask having an aperture. (6.76 mm^2) External quantum efficiency (EQE) was measured by a specially designed EQE system (PV measurement Inc.) with 75 W Xenon lamp (USHIO, Japan) as a source of monochromatic light. The photoluminescence spectra was obtained by a spectroflourometer(Horiba, Flouoromax-4)

Experimental setup for ion generation and deposition[35]

The whole chamber contains two connected chambers: the ion generation(IG) chamber and the ion deposition(ID) chamber. The IG chamber has cylindrical shape with 30 mm diameter and and 35 mm height. It is made of transparent acrylic which makes it possible to see the state of corona discharge during experiment. Stainless steel pin and plate creates highly asymmetric electric field in the chamber, when a bias voltage is applied between the pin and the plate. Gas 1 can flow into the chamber through an inlet on the side wall. The polarity of generated ions is determined by the polarity of applied voltage to the pin. The current of generated ions was measured by Faradaycup electrometer (Keithley Sub-femtoamp romote sourcemeter, 6430). A high-voltage supply (FuG ElektronikGmbH,

HCP140-12500) apply voltage to the pin and the substrate in the ID chamber.

The ions generated in the IG chamber flows through a 115 mm long pipe with a 1.5mm diameter that connects the IG and ID chambers. A tee tube connected to this pipe introduces Gas 2 into the system. The flow rates of Gas 1 and 2 are both controlled by mass flow controllers (MKS instruments, MFC Controller 247D, MFC 1179A). The negatively (postively) charged gas ions are electrostatically attracted and deposited on the positively (negatively) biased substrate with the bias voltage of 2kV (-2kV).

Corona ion generation

Nitrogen gas inflow with the flow rate of 2 lpm was transformed into positive nitrogen ions by applying 4.2 kV to the pin. The electric current of generated nitrogen ions was measured to be 20.6-25.8 pA, which is indicative of positive ion generation. To generate negative ions, we used hydrogen gas with the flow rate of 2 lpm and applied negative bias (-1.55 kV) to the pin, whcich generates the current of -3.2 ~ -4.8 pA. (see Table 2.3)

Atmosphere control

To maintain the condition of the air inside the chamber at constant, the flow rate of Gas 2 was controlled by MFC and set as 1.5 lpm throughout the measurements. Nitrogen, dry air, humidified nitrogen and air were used as Gas 2. Nitrogen and hydrogen gases are highly purified by 99.999%, and dry air consists of 80% of nitrogen (99.999%) and 20% of oxygen(99.995%). Gas 2 passes through a water bubbler that controls the humidity in the chamber. The relative humidity was measured by portable multifunction data-logger(Delta OHM, Data logger DO9847, Temp&Humidity probe HP474AC) at the gas exit of deposition chamber.

		Flow rate(L m^{-1})	Current of generated ion (pA)	Applied voltage
Gas1	Nitrogen	2	20.6 ~ 25.8	4.2kV (0.009 mA)
	Hydrogen	2	-3.2 ~ -4.8	-1.55kV (-0.4 mA)
Gas2	Nitrogen	1.5		
	Dry air	1.5	-	

Table 2.3 The parameters for ion generation and data obtained from MFC controller and Faradaycup electromer.

Topography and Kelvin probe force microscopy

All the samples for topography and Kelvin probe force microscopy measurements were prepared on ITO glass substrates. The perovskite films were spin-coated on the ITO glass and ITO/C_{60} substrate. The ion-treated sample was prepared by depositing N_2 positive corona ion for 1 hr on the ITO/perovskite substrate. In the case of the light-illuminated sample, the ITO/C_{60} substrate was used in order to measure positive charge accumulation profile. After one sun illumination for 1 hr, the sample was measured under light on or off during KPFM operation (Figure 2.11).

Topography and Kelvin probe force microscopy (KPFM) signals were measured by using an atomic force microscope (MFP-3D, Asylum Research) with a Pt-coated tip with the spring constant of 2 nN nm^{-1} and the resonant frequency of 77 kHz. For each line scanning, topography was first measured and successively the surface potential was measured while scanning the same line at a fixed distance above the sample surface. The tip was positioned sufficiently away from the substrate (as far as 20 nm) in order to exclude the corss-talk artefacts from topography footprints. The surface potential was measured using an active electronic feedback circuitry: the bias voltage to the tip was modulated in order to equate

the potential of the tip with that of the surface, resulting in minimum vibration amplitude of the AFM tip at the fundamental frequency. A 150W halogen bulb with single fiber light guide was used for illumination.(Figures 2.9 and 2.11)

An atomic force microscope (Park systems, NX10) was used to obtain topography and surface potential images of perovksite films. In the ion-treated sample, nitrogen cations produced by corona discharge were deposited on the perovskite film coated on the ITO substrate for 1 hr. In the case of the light-treated sample, the profile of positive charge accumulation in the perovskite film coated on the ITO/C_{60} substrate was mesured after one sun illumination for 1 h.(Figures 2.12-2.14)

Computational details

All DFT calculations were performed with the Vienna *ab initio* simulation package (VASP, version 5.3.5),[50] and the results were visualized by the VESTA (visualization for electronic and structural analysis) and the VMD (Visual Melecular Dynamics) program[51,52]. The projector augmented wave (PAW) method[53,54] was used to describe the electron-ion interaction with the kinetic energy cutoff set to 520.0 eV for the plane waves. We used the Perdew-Burke-Ernzerhof (PBE) exchange-correlation

functional[55] and weak van der Waals interactions were considered by the zero damping DFT-D3 method of Grimme[56]. We performed spin-unpolarized calculations for the neat, water-, and nitrogen-covered $MAPbI_3$ surface but spin-polarized calculations for the oxygen-covered $MAPbI_3$ surface to consider the triplet-state nature of the ground state oxygen. The Brillouin-zone was sampled with a Γ-centered (4 × 1 × 4) Monkhorst-Pack k-point grid for structural relaxation and only a single Γ-point was used for the AIMD simulation. All AIMD simulations were performed in the canonical ensemble using Nosé thermostat with a temperature of 298 K. The total simulation time of each trajectory was 2 ps with a 2 fs time-step. The charge of molecules were obtained by summing atomic charges from Bader population analysis.[57]

The reference structure of $MAPbI_3$ unit cell was constructed from the experimentally determined geometry. We reproduced the experimentally verified orthorhombic $MAPbI_3$ unit cell that consists of four $MAPbI_3$ units (a = 8.836 Å , b = 12.580 Å , c = 8.555 Å)[58], and made little modification on lattice parameters to make the tetragonal crystal structure of $MAPbI_3$ at 25 ℃ ($a = c$ = 8.852 Å , b = 12.444 Å)[58]. The reference unit cell was fully relaxed at first, whose surface was defined by inserting a large vacuum layer (15 ~ 25 Å) along the b-axis to prevent the interaction with upper periodic

unit cells. To check the effect of vacuum potential, AIMD simulations were performed for neat $MAPbI_3$ surface by changing the vacuum thickness.(Figure 2.23) For the 5 Å case (Figure 2.23a), movable atoms gradually rise up toward the bottom of the upper unit cell because of the potential in the vacuum region. However, for 10 ~ 25 Å cases (Figures 2.23b ~ e), it is clearly shown that no atoms are moved up into the vacuum layer, which implies little interaction between unit cells. Therefore there are negligible dipole effect to simulations. Initial geometries for AIMD simulation were prepared by placing 5 H_2O, 4 N_2, 4 O_2, or a null layer at appropriate positions of the $MAPbI_3$ surface (same locations chosen for N_2 and O_2). After the initial relaxation in the neutral state, the simulation started with a net charge of +1, 0, or −1 in the unit cell by ejecting (+1) or injecting (−1) an electron. In all surface relaxations and simulations, two $MAPbI_3$ units at the bottom of the unit cell were rigidly fixed while all other atoms that compose the upper two $MAPbI_3$ units and the adsorbates were allowed to move.

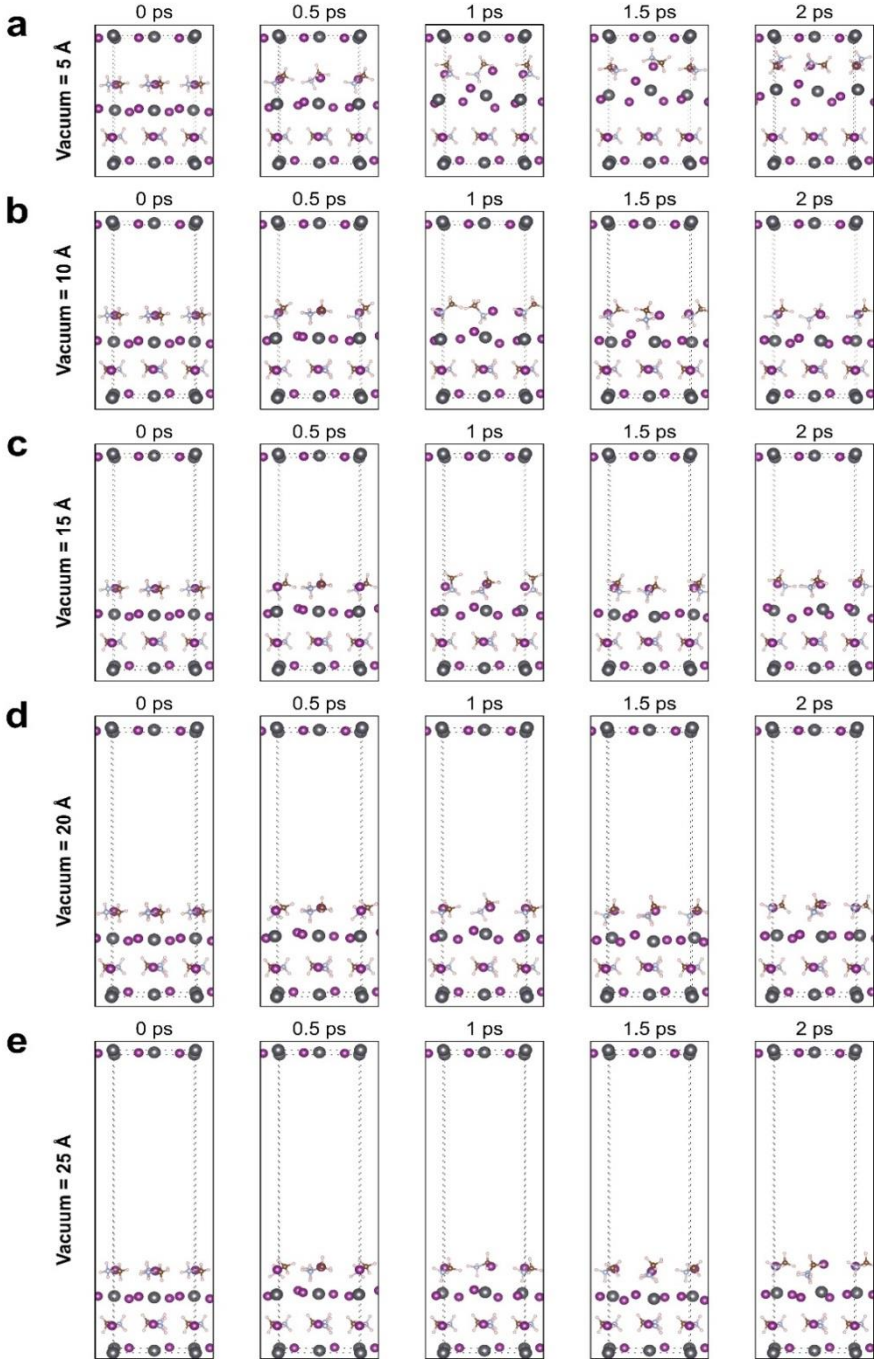
a
Vacuum = 5 Å
0 ps
0.5 ps
1 ps
1.5 ps
2 ps
b
Vacuum = 10 Å
0 ps
0.5 ps
1 ps
1.5 ps
2 ps
c
Vacuum = 15 Å
0 ps
0.5 ps
1 ps
1.5 ps
2 ps
d
Vacuum = 20 Å
0 ps
0.5 ps
1 ps
1.5 ps
2 ps
e
Vacuum = 25 Å
0 ps
0.5 ps
1 ps
1.5 ps
2 ps

Figure 2.24 a, Temporal snapshots of the AIMD simulated atomic trajectories of $MAPbI_3$ crystal in neutral with vacuum thickness of a, 5 Å , b, 10 Å , c, 15 Å , d, 20 Å , and e, 25 Å .

Chapter 3.

Degradation mechanism of other compositional perovskite material

Published in *Nature Communications*, 2016, **7**, 13422

Updated in arXiv:1709.04130

3.1. Introduction

Organic-inorganic hybrid perovskite materials have lately drawn global attention due to their excellent photovoltaic performance.[2,28,59-62] The organic cations of the material play an important role in photovoltaic properties such as bandgap, exciton binding energy, and carrier lifetime[44,63,64], but they also pose an obstacle in the commercialization of perovskite-based solar cells because of their instability. In general, organic compounds can undergo a chemical reaction with oxygen and atmosphere water, which can be activated under certain conditions such as high temperature or light irradiation. Indeed, the hybrid perovskite materials have shown fast decomposition into organic and inorganic components in the presence of water and oxygen under light irradiation[16,18,19,24,25,30,46,65], which casts serious but

reasonable doubts to the prospect of using such perovskite materials as an active layer in photoelectric devices.

There have been many studies that attempted improving the chemical stability of perovskite materials, mostly by identifying a single source of instability such as water[15,18,19,30], oxygen[16,24,25,46], light[18,65,66], iodine vapor[67] and electric field[18,23]. Recently, we reported a new degradation mechanism based on the electrostatic charges trapped in the perovskite crystal. These charges that were originally generated by light absorption and then trapped mostly along the grain boundaries, were shown to trigger the irreversible degradation of perovskite material in the presence of moisture, which was attributed to the charge driven deprotonation of organic cations. While no similar charge-driven mechanism has been proposed for oxygen-induced degradation of perovskite, we note that the recent discovery of $MAPbI_3$ perovskite suffering from irreversible degradation in the presence of only oxygen without moisture under light soaking[16,24,25,46] indicates that oxygen and water may individually possess different chemical pathways for perovskite degradation.

To dig into this charge driven degradation mechanism, we investigated controlled stability experiments both for commonly used $CH_3NH_3PbI_3$ ($MAPbI_3$) that is known to form structurally distorted

tetragonal crystals and a new mixed perovskite material having more enhanced structural stability. The crystal structure of perovskite can become more stable by increasing the tolerance factor close to unity by incorporating other organic cation and halide anion with different ion sizes.[68,69] Addition of formamidinuim (FA) cation and bromide (Br) anion could not only structurally stabilize the perovskite materials by increasing tolerance factor towards one for inducing cubic crystals, but also enhance their photovoltaic performance by broadening absorption spectrum.[70,71] Although several studies on mixed cation and/or halide anion system of $MA_xFA_{1-x}PbI_yBr_{3-y}$ have been suggested[5,70,71], they focused on the performance aspect, not the stability aspect. Therefore, a new effort is required to develop new composition perovskite ensuring both stability and high performance. In this work, we developed a new mixed $MA_{0.6}FA_{0.4}PbI_{2.9}Br_{0.1}$ perovskite ensuring both high performance and stability via lewis-base adduct method.[3] Later, it will be shown that this new mixed perovskite still degrades although its degradation speed is slower than the case of conventional $MAPbI_3$ and the irreversible degradation of both perovskites is triggered by trapped charges.

We also investigated the degradation mechanism of $FAPbI_3$ which has better absorption property and stability against light and themal stress than $MAPbI_3$. A study of the degradation mechnism of $FAPbI_3$ is lacking

compared to $MAPbI_3$. Currently, the most anticipated degradation foute of $FAPbI_3$ is the phase trasition fromm blakc alpha phase to yellow delta phase.[8,72,73] Phase transition from alpha phase to delta phase is commly known to occur under high relative humidity condition at room temperature. In this study, we found that $FAPbI_3$ also degraded by trapped charges with water or oxygen, but it has different degradation route than $MAPbI_3$. In the case of puer $FAPbI_3$ it was confirmed that phase transition to delta phase occured when there is sufficient water, and we predicted that the reason of phase transition is due to strong interation between FA organic cation and H_2O molecules. It is also confirmed that the phase is stabilized by adding a little cs to the $FAPbI_3$. If the mositure is not sufficient to phase transition, we found that the decomposition of $FAPbI_3$ occured by trapped charge.

On the other hand, in the oxygen atmosphere, we found that the decomposition of $FAPbI_3$ occured and the phase transition to delta phase hardly occred. When the decomposition of FAPbI3 occurs, it finally changes to PbI_2 and the degradation route was perdicted by AIMD simulation. In other words, $FAPbI_3$ is also degraded by trapped charge as MAPbI3 but predicted to have another degradation mechanism due to the crystal structure and characteristics of FA .

3.2. Results and discussion

In a mixed cation and halide anion system of Pb-based perovskite, $APbX_3$, the Goldschmidt tolerance factor t is defined in terms of the average radii of ions as follows.

$$t = \frac{\overline{r_A}+\overline{r_x}}{\sqrt{2}(\overline{r_{Pb}}+\overline{r_x})} \quad \text{... (1)}$$

where $\overline{r_A}$, $\overline{r_X}$, and $\overline{r_{Pb}}$ are the average radii of the cation, anion, and lead ions, respectively. The I^-, Br^- and Pb^{2+} ions have a spherical shape and the radii of these ions have been measured in previous works.[74] In constrast, it is difficult to precisely estimate the radii of the organic cations perched on the A site due to their non-spherical shape and rotational motion, nevertheless, several groups already reported the calculated effective ion radius of both MA^+ and FA^+ cation.[64,75-77] By using equation 1 and the suggested ionic radii (r_{MA+}= 0.18 nm, r_{I-}= 0.22 nm, r_{Pb2+}= 0.12nm), the tolerance factor of $MAPbI_3$ is calculated to be 0.83[77], indicating that MA^+ cations are too small to fit into the interstices between PbX_6 octahedra. This mismatch causes crystal distortion, and consequentially $MAPbI_3$ perovskite have unstable tetragonal crystal structure.[78,79] By partially replacing MA^+ and I^- to relatively larger FA^+ and smaller Br- ions respectively, crystal distortion can be alleviated to produce more stable cubic structure with the tolerance factor between 0.9-

1.[68] Simple calculation reveals that replacing I^- to Br^-(r_{Br-} = 0.196 nm) only marginally affects the perovskite crystal structure as the tolerance factor of $MAPbBr_3$ is only 0.01 higher than that of $MAPbI_3$. On the other hand, replacing MA to FA cation can significantly alter the crystal structure because FA cations are expected to be much larger than MA cations. The exact radius of FA cation is still controversial,[68] but considering that $FAPbI_3$ can possess not only non-perovskite yellow δ-phase with hexagonal crystal structure (t >1) but also black perovskite α-phase with cubic structure (0.9 < t < 1), it can be speculated that the tolerance factor of $FAPbI_3$ would be around 1. The radius of FA cation r_{FA+} is estimated to be around 0.26 nm from these speculations and equation 1. The tolerance factor of mixed cation system, $MA_xFA_{1-x}PbI_3$, is calculated as a function of the ratio x as shown in Figure 3.1. This relation suggests that the x values between 0.2 and 0.6 lead to the most stable cubic crystal structure, as the resulting tolerence factor lies between 0.9 and 1.

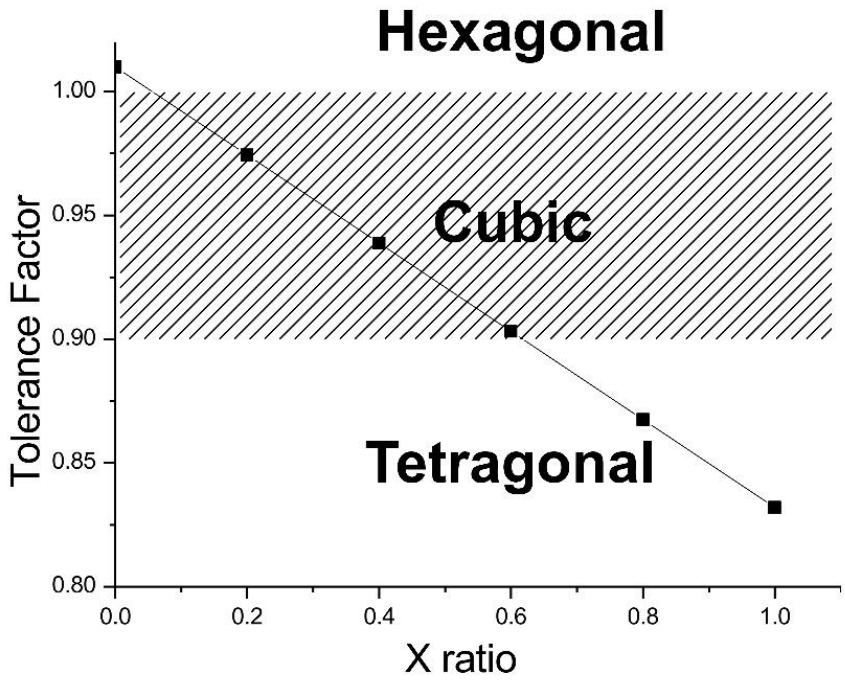

Figure 3.1 Dependence of the Goldschmidt tolerance factor on the MA fraction (x) of $MA_xFA_{1-x}PbI_3$

We measured X-ray diffraction(XRD) patterns of five types of mixed perovskite films (x= 1, 0.8, 0.6, 0.4, 0.2) coated on the ITO glass in order to compare their stability. Figure 3.2a, b show the XRD patterns of the fresh and degradaded samples, respectively. The perovskite films were degraded in the chamber (relative humidity (RH) ~ 50%) for 10 hours under one sun illumination. The peak originating from PbI_2 at 12.7 degrees intensively appears in the case of MAPbI3 (x=1), and the peak of non-perovskite δ-phase FAPbI3 at 11.7 degrees appears for $x < 0.4$, which indicates severe instability to water vapor.[8,80] (Figure 3.2c, d) These observations suggest that the most stable composition would be $MA_{0.6}FA_{0.4}PbI_3$ (x=0.6), which still posesses the tolerance factor ensuring the cubic crystal structure.

We also fabricated the full devices with the ITO/C_{60}/Perovskite/Spiro-MeOTAD/Au structure in order to find the optimal composition with respect to the photovoltaic performances in mixed perovskite $MA_xFA_{1-x}PbI_yBr_{3-y}$. Figure 3.3a, b summarize the PCEs as a function of the MA^+ fraction(x) and the Br^- fraction(3-y), respectively. As a result, the $MA_{0.6}FA_{0.4}PbI_{2.9}Br_{0.1}$–based devices were shown to the best performance. Considering that MA:FA=0.6:0.4 is the best composition for stability, we concluded that $MA_{0.6}FA_{0.4}PbI_{2.9}Br_{0.1}$ would be the best composition in terms of both performance and stability in mixed perovskite systems.

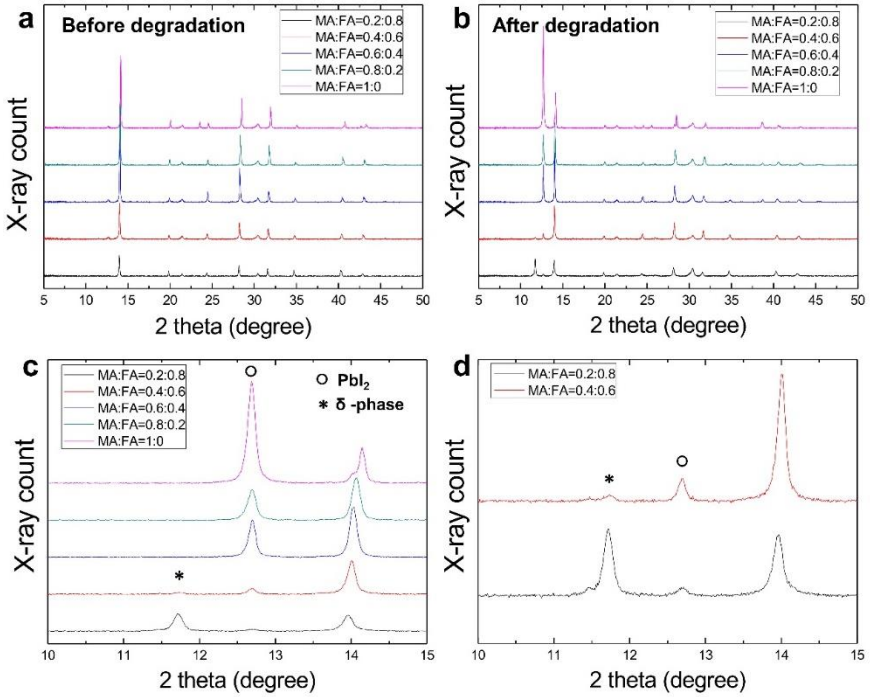

Figure 3.2 X-ray diffraction patterns of five different mixed perovskite films coated on ITO glass (x=0.2 (black), 0.4 (red), 0.6 (blue), 0.8 (green), and 1 (pink)) (a) before and (b) after degradation under one sun illumination at 50 % relative humidity for 10 hours. (c) Magnified XRD patterns around the peaks originating from PbI_2 and non-perovskite δ–phase. (d) Magnified XRD patterns for x=0.2 and 0.4

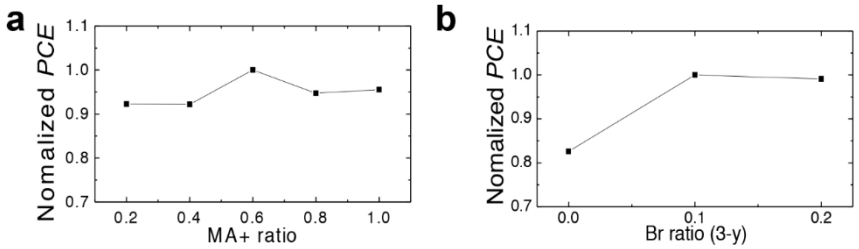

Figure 3.3 Dependence of the normalized PCEs of ITO/C_{60}/Perovskite/Spiro-MeOTAD /Au device on (a) the MA+ fraction (x), and (b) the Br- fraction (3-y)

Figure 3.4a showed the degradation patterns of our mixed $MA_{0.6}FA_{0.4}PbI_{2.9}Br_{0.1}$ for two days in the dark condition with relative humidity (RH) 90 %. The absorption spectra of our mixed $MA_{0.6}FA_{0.4}PbI_{2.9}Br_{0.1}$ perovskite were hardly changed with the high relative humidity condition (see Figure 3.5) and XRD patterns were the same after two days (see Figure 3.6). This indicates our mixed composition perovskite would be more resistible to become hydrated than distorted tetragonal perovskite $MAPbI_3$. It is likely that water molecules could penetrate more easily into the distorted tetragonal $MAPbI_3$ than into the more compact cubic crystal structure of $MA_{0.6}FA_{0.4}PbI_{2.9}Br_{0.1}$. A slight change of the absorption spectra shown in Figure 3.4b indicates a slow hydration could still happen to our mixed perovskite under 90 % RH. However, $MA_{0.6}FA_{0.4}PbI_{2.9}Br_{0.1}$ also perovskites showed irreversible degradation under light soaking at RH 20 % (see Figure 3.4b). It is interesting to note that under light soaking, our mixed perovskite degrades more slowly than the conventional $MAPbI_3$.

Moreover, the structurally distorted (conventional) $MAPbI_3$ film was degraded more quickly than the mixed stable $MA_{0.6}FA_{0.4}PbI_{2.9}Br_{0.1}$ under the same moisture and ion deposition level (Figure 3.6).

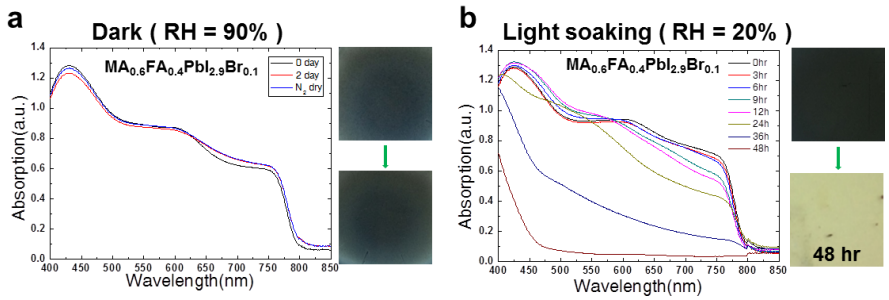

Figure 3.4 Absorption spectra of (a) $MA_{0.6}FA_{0.4}PbI_{2.9}Br_{0.1}$ perovskite films under dark conditions at 90% relative humidity. Time evolution of absorption spectra of (b) $MA_{0.6}FA_{0.4}PbI_{2.9}Br_{0.1}$ during light soaking at 20% relative humidity. Pictures of the perovskite films before and after aging are shown on the left side of each figure.

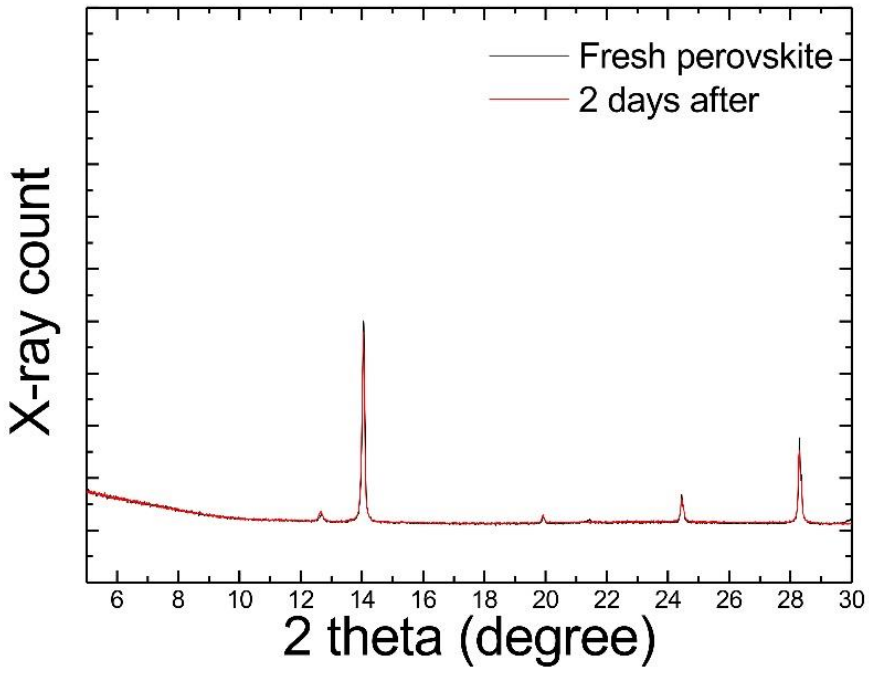

Figure 3.5 XRD patterns of the perovskite film before (red) and after (black) aged at 90% relative humidity for 2 days.

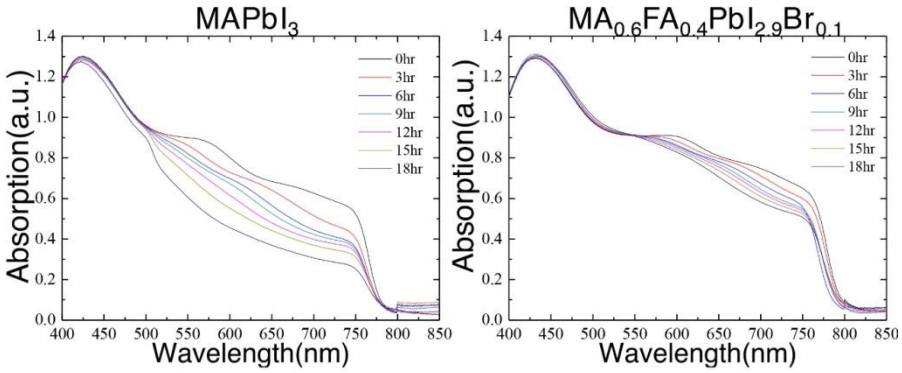

Figure 3.6 Comparison of the degradation rates of $MAPbI_3$ and $MA_{0.6}FA_{0.4}PbI_{2.9}Br_{0.1}$ perovskite films at 40% relative humidity with positive nitrogen ion deposition. Absorption spectra were measured at an interval of 3 hr.

We examined that the characteristics of $MA_{0.6}FA_{0.4}PbI_{2.9}Br_{0.1}$-based solar cells which has ITO/C_{60}/perovskite/Spiro-MeOTAD/Au structure. Figure 3.7a show J-V curves for $MA_{0.6}FA_{0.4}PbI_{2.9}Br_{0.1}$ perovskite solar cells, which demonstrates hysteresis-less performance of the best PCE of 20.2%. The best PCE value was averaged from the J-V curves of forward and reverse scan, which is in agreement with 20.2% of steady-state efficiency shown in Figure 3.7b. The integrated Jsc estimated from external quantum efficiency (EQE) was also well-matched with the measured Jsc as shown in Figure 3.7c. Histograms of the short-circuit current (Jsc), the open-circuit voltage (Voc), the fill factor (FF) and the efficiency of 47 cells are shown in Figures 3.7d, e, f, g. The photovoltaic characteristics of these cells were highly reproducible with a small standard deviation, and the average values are Jsc = 24.34 mA cm^{-2}, Voc = 1.058 V, FF = 0.743, and PCE = 19.12%, respectively. This would be the best performance of low-temperature processed perovskite solar cells without using mesoporous TiO_2. As seen in Figures 3.4 and 3.6, our new mixed composition perovskite has improved efficiency and stability than $MAPbI_3$, but the $MA_{0.6}FA_{0.4}PbI_{2.9}Br_{0.1}$ also degraded by trapped charge in the presence of water molecules. $MA_{0.6}FA_{0.4}PbI_{2.9}Br_{0.1}$ also decomposited to the PbI_2 like $MAPbI_3$.(see Figure 3.8)

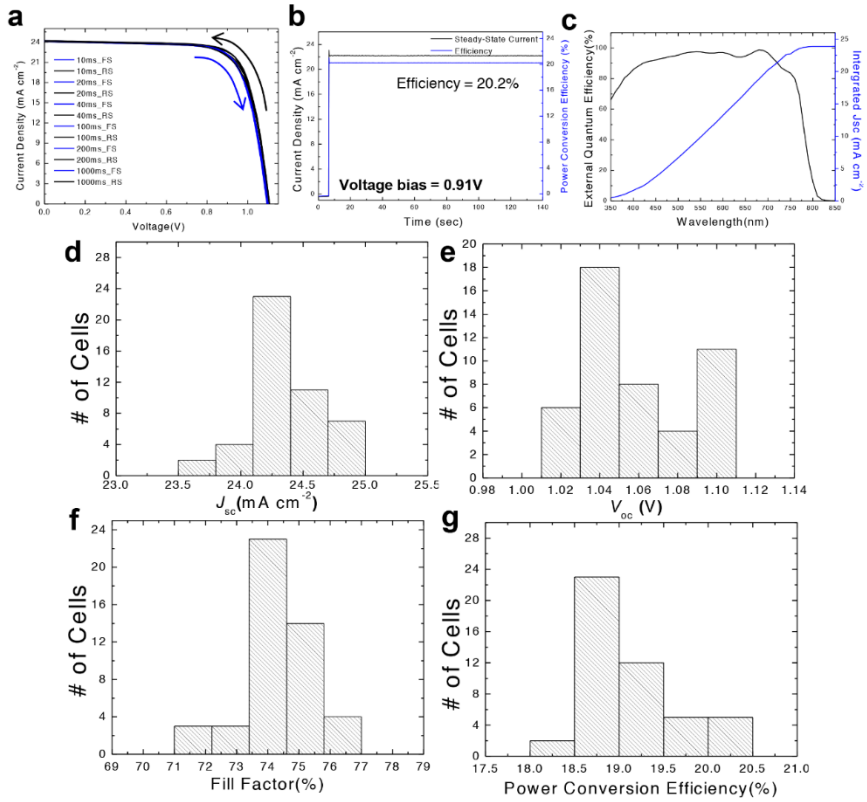

Figure 3.7 Photovoltaic performance characteristics. (a) *J-V* curves of the best-performing device measured at various sweep delay times. (b) Stabilized photocurrent density (black) and power conversion efficiency (blue) measured at a bias voltage of 0.91V for 140 seconds. (c) External quantum efficiency (EQE) spectrum and the integrated J_{sc} estimated from the measured EQE. Histograms of (d) short-circuit current density (J_{sc}), (e) open-circuit voltage (V_{oc}), (f) fill factor (FF), and (g) power conversion efficiency (*PCE*) of 47 cells

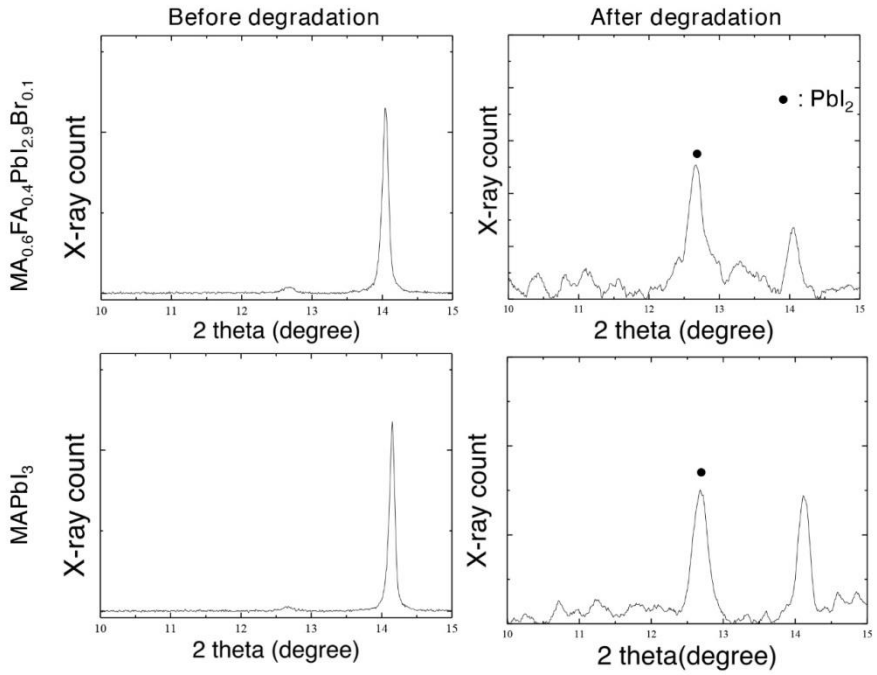

Figure 3.8 XRD patterns of the $MA_{0.6}FA_{0.4}PbI_{2.9}Br_{0.1}$ and $MAPbI_3$ film before and after degradation by trapped charges in the presence of moisture.

Considering the structural distortion in the $MAPbI_3$ crystal[69,78,79], the region between the PbI_6^- octahedron units may be the weakest point of infiltration for external gas molecules. Therefore, structural stabilization of perovskite by tuning tolerance factor to yield a cubic phase structure may benefit its chemical resistance against water or oxygen molecules. In view of the improved stability of our structurally more stable multi-component perovskite $MA_{0.6}FA_{0.4}PbI_{2.9}Br_{0.1}$ against water (see Figures 3.4, 3.6 and 3.9), we attempted to check its stability against oxygen as well. We prepared the $MA_{0.6}FA_{0.4}PbI_{2.9}Br_{0.1}$ film using our three different experimental apparatuses(Figure 2.7) and measured their absorption spectra and change thereof in 24 hours (Figures 3.10). Surprisingly, these perovskite films showed no sign of degradation under oxygen exposure after 24 hours even with charge deposition and light soaking. To further confirm the improvement in material stability, we measured the photovoltaic conversion efficiency (PCE) of (unencapsulated) devices stored under one sun irradiation in pure oxygen for 36 hours (Figure 3.11 and 3.12), which showed a dramatic improvement over conventional $MAPbI_3$ based device raising the prospect of these multi-component perovskite materials for long-term stability.

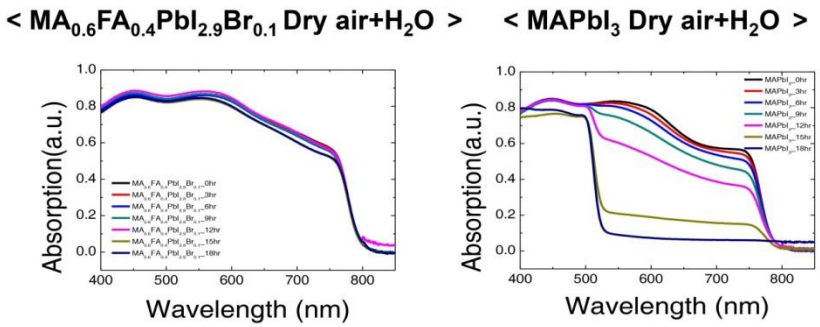

Figure 3.9 Time evolution absorption spectra of $MA_{0.6}FA_{0.4}PbI_{2.9}Br_{0.1}$ (left) and $MAPbI_3$ (right) films aged under one sun illumination in humidified dry air for 18 hours.

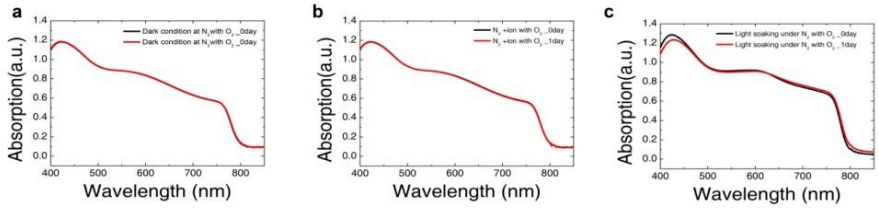

Figure 3.10 Absorption spectra of $MA_{0.6}FA_{0.4}PbI_{2.9}Br_{0.1}$ film measured before and after 1 day of aging with dry air, a, under dark condition, b, with nitrogen cation deposition, and c, under one-sun irradiation.

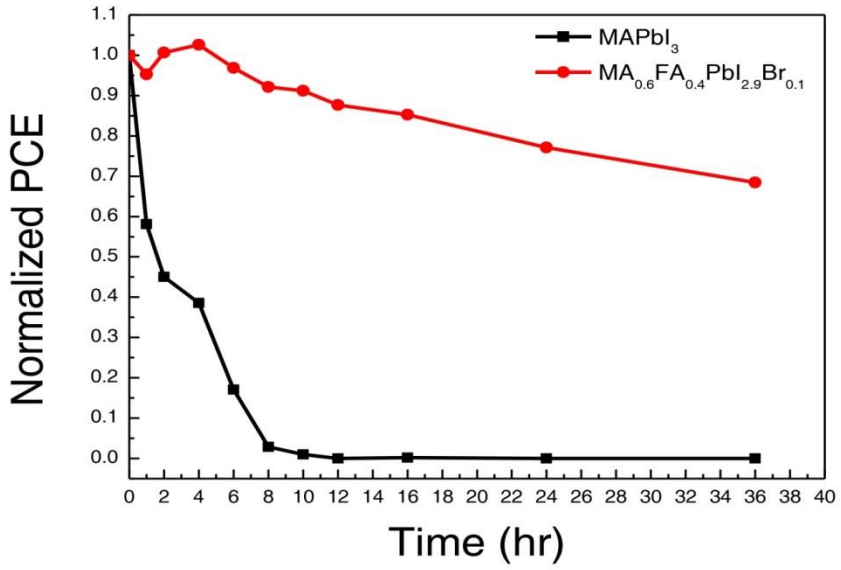

Figure 3.11 Normalized PCEs of $MAPbI_3$ and $MA_{0.6}FA_{0.4}PbI_{2.9}Br_{0.1}$ perovskite solar cell under one-sun irradiation with a continuous flow of pure oxygen. In these devices, C_{60} and Spiro-MeOTAD were used for ETL and HTM, respectively.

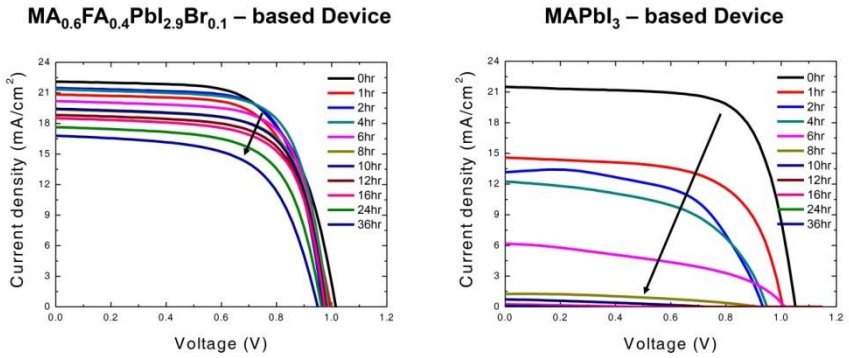

Figure 3.12 Time evolution of J-V curves of $MA_{0.6}FA_{0.4}PbI_{2.9}Br_{0.1}$ (left) and $MAPbI_3$ (right) based devices aged under one sun illumination in 100% oxygen ambience for 36 hours.

Next, we investigated the degradation mechanism of $FAPbI_3$ material. Figure 3.13 shows the degradation patterns of pure $FAPbI_3$ film in the presence of moisture. First, in Figure 3.13a, 0.5ml of water was placed on the bottom of sealed chamber full filled with humidified nitrogen. The relative humidity of this chamber was over 90%. When pure $FAPbI_3$ film was placed in this chamber which has lots of water molecules, the black film changed to yellow semi-transparent film. The XRD patterns of yellow film had only δ-phase $FAPbI_3$ peaks and there were no α-phase $FAPbI_3$ peaks.(Figure 3.14) That is, in the case of pure α-phase $FAPbI_3$ under high relative humidity condition, the phase transition occurred faster than the decomposition of $FAPbI_3$ material occurred. For the experiment under low relative humidity condition(about 35%), we used the apparatus as shown in Figure 2.7. As seen in Figure 3.13b and c, in the case of pure α-phase $FAPbI_3$ under low relative humidity condition, the decomposition of $FAPbI_3$ material occurred. The inset figure shows the degraded films at respective condition. When phase transition occurred, the film had very light yellow color. On the other hand, when the $FAPbI_3$ film was decomposed, the film had dark yellow and a little purple color.

This can be seen as PbI_2 and I_2 resulted in decomposition. Thus, when trapped charge is present in $FAPbI_3$, decomposition occurs in the same as $MAPbI_3$.However, when moisture is sufficient, the phase

transition occurs differently from $MAPbI_3$. This phase transition can also be predicted by the Goldschmidt tolerance factor. In the case of $FAPbI_3$, the Goldschmidt tolerance factor is more than 1, so it is difficult to maintain the stable cubic structure at room temperature. So AIMD simulation was performed to further analyze the degradation mechanism of $FAPbI_3$. As can be seen in figure 3.15, when the trapped charge was presented, the degradation route of $FAPbI_3$ was almost similar to that of $MAPbI_3$. In positively charged crystal, the FA^+ cation was solvated by the interaction between H_2O molecules and FA^+ cation. As the result of solvation, the FA^+ cation was chipped off from the perovskite crystal. In negatively charged crystal, the I^- anion was elevated from the perovskite crystal. Rather, the unusual phenomenon different from $MAPbI_3$ appeared when there was no trapped charges. As mentioned above, in Figure 2.17b, the water molecules evolved out of the $MAPbI_3$ surface in the neutral case. However, the water molecules remained near or inside of $FAPbI_3$ surface especially near the FA^+ cation.(Figure 3.15) It means that there is a strong interaction between FA^+ cation and H_2O molecules. When $FA{\bullet}H_2O$ state is generated by strong interaction, the effective radius of organic cation of perovskite becomes bigger.

Therefore, the Goldschmidts tolerance factor of the $FAPbI_3$ with water molecules is larger than that of $FAPbI_3$ without water, and it is

expected that the phase transition to the δ-phase will occur more easily. The structural instability of FAPbI3 can be solved by doping Cs^+ cation.[8,9,68] Cs-doped $FAPbI_3$ has a small Goldschmidts tolerance factor and can maintain a stable cubic phase. It was confirmed again in the experimental results. Figure 3.16a is the absorption spectra and picture of the $FAPbI_3$ films aging for one day without light illumination in the ambient air condition (about RH 50%). In the case of pure $FAPbI_3$, the phase transition occurred, but in the case of Cs-doped $FAPbI_3$(5% doping, $FA_{0.95}Cs_{0.02}FAPbI_3$), there was no changes and the film retained the cubic phase. In addition, the degradation rate of Cs-doped $FAPbI_3$ was much slower than that of pure $FAPbI_3$ under low relative humidity condition.(Figures 3.16b and c) It is suggested that Cs-doped $FAPbI_3$ retains the cubic structure better, thus the penetration of H_2O molecules are prevented.

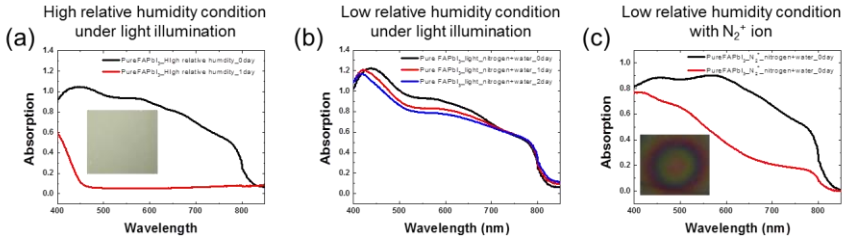

Figure 3.13 Absorption spectra of pure $FAPbI_3$ aged under light illumination at (a) high relative humidity(>90%) condition and (b) low relative humidity condition(about 35%) and positive nitrogen ion deposition at (c) low relative humidity condition. The inset figures are the degraded films under respectively conditions.

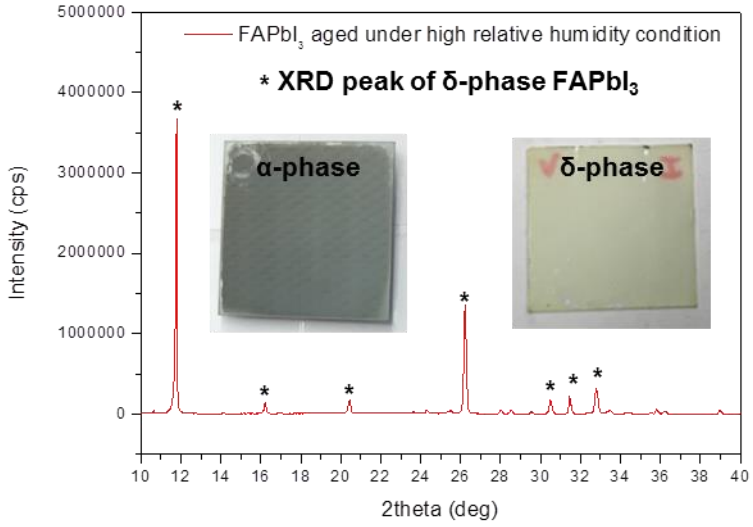

Figure 3.14 XRD patterns of $FAPbI_3$ film aged under high relative humidity condition. The inset figures are the picture of film before (α-phase) and after (δ-phase) aging.

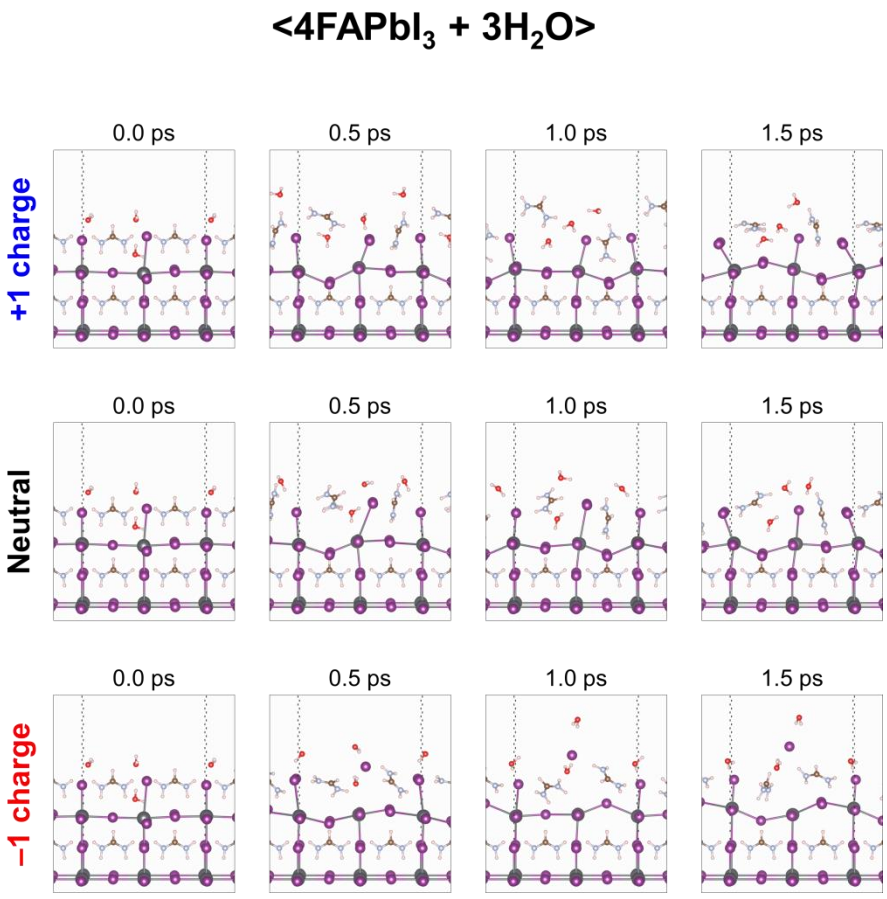

Figure 3.15 Temporal snapshots of the AIMD simulated atomic trajectories of 3 H_2O molecules and $FAPbI_3$ cubic crystal with a charge of +1, 0, and -1. All simulations star with the same initial geometry at 0ps.

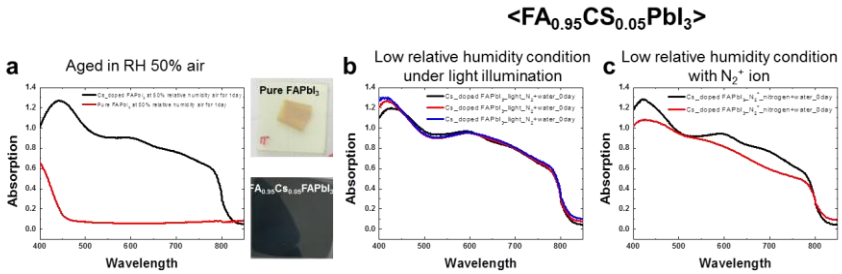

Figure 3.16 (a) Absorption spectra of Pure $FAPbI_3$ and Cs-doped $FAPbI_3$ aged in RH 50% air for 1day. Absorption spectra of Cs-doped $FAPbI_3$ aged under (b) light illumination and (c) positive nitrogen ion deposition at low relative humidity condition

Figure 3.17 shows the absorption spectra of pure $FAPbI_3$ aged under 99.995% oxygen. First, we found that the oxygen did not degrade the $FAPbI_3$ without trapped charges. In Figure 3.17a, the pure $FAPbI_3$ film was placed in the sealed dark chamber fulfilled with 99.995% oxygen for 2days. The absorption spectra of $FAPbI_3$ was hardly changed. Next, we also used the apparatus shown in Figure 2.7b and c for generation charges. As seen in Figures 3.17 b and c, the absorption spectra of $FAPbI_3$ changed rapidly both case of light illumination and positive nitrogen deposition with oxygen. Unlike the case of high relative humidity condition, the phase transition to δ-phase hardly occurred under oxygen condition. The XRD patterns of $FAPbI_3$ film degraded under light illumination at oxygen condition has only PbI_2 peaks and no δ-phase peaks.(Figure 3.18) It is also confirmed that the degraded film has dark yellow color. From these results, when trapped charges are formed on the perovskite film under oxygen, pure $FAPbI_3$ was decomposed to PbI_2.

We also carried the AIMD simulations in order to analyze the degradation mechanism of $FAPbI_3$ with oxygen.(Figure 3.19) In this simulation, the routes of degradation of $FAPbI_3$ were different from that of $MAPbI_3$. When there are no charges (Neutral), oxygen molecules escaped from the $FAPbI_3$ surface. However, when trapped charges existed, oxygen molecules affected to the $FAPbI_3$ perovskite

crystal. In the case of $MAPbI_3$ with oxygen, it was founded that the strong oxide bonding between Pb-O or I-O was formed.(Figure 2.23) We expected that these generated oxide bond would be loosen the perovskite crystal bonds, as the result the perovskite crystal may have collapsed. On the other hand, in the case of positively charged $FAPbI_3$ crystal, oxygen molecule took place by replacing the FA^+ cations. It was expected that the leached FA^+cation was detached from the perovskite crystal, as a result, the $FAPbI_3$ crystals collapsed. In the case of negatively charged $FAPbI_3$ crystal, the strong bond between Pb and O was formed. The bond length between Pb and O was 2.41Å at 2ps. It was also confirmed that the superoxide was generated in negatively charged case. The oxygen which interact with Pb had -0.62 charges, so it wass thought to be super oxide. I^- anion was pushed out from the perovskite crytal because it has -0.73 negative charges. Due to these results, the crystal of $FAPbI_3$ would be destroyed under oxygen condition.

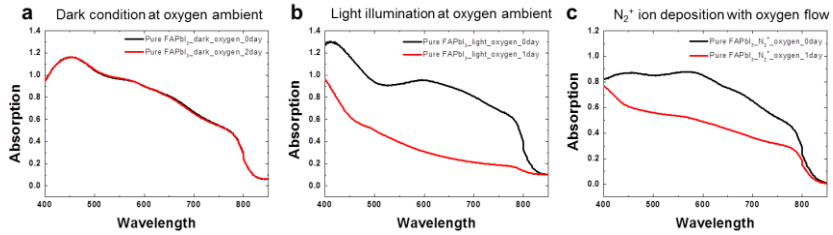

Figure 3.17 Absorption spectra of pure $FAPbI_3$ aged under (a) dark condition, (b) light illumination (c) and positive nitrogen ion deposition at 99.995% oxygen ambient.

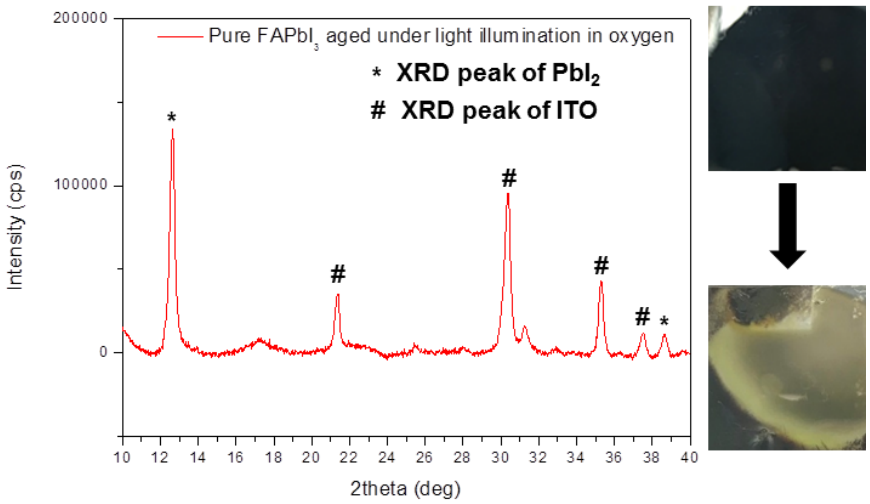

Figure 3.18 XRD patterns of $FAPbI_3$ film aged under 99.995% oxygen ambient. The figures are the picture of film before (and after degradation.

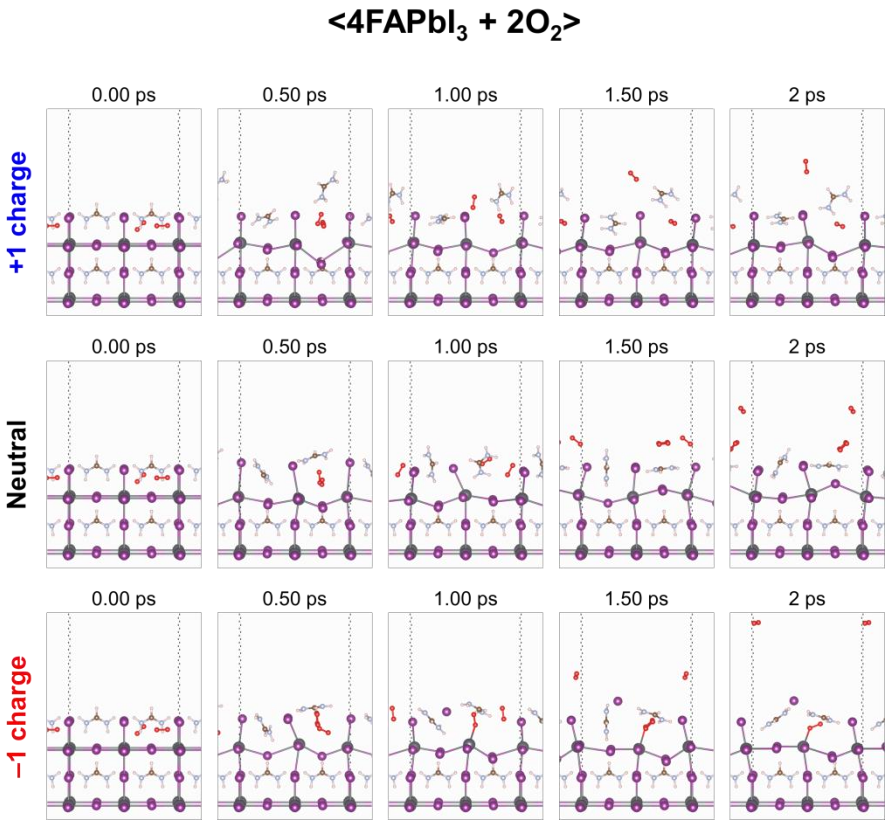

Figure 3.19 Temporal snapshots of the AIMD simulated atomic trajectories of 2 O_2 molecules and $FAPbI_3$ cubic crystal with a charge of +1, 0, and -1. All simulations star with the same initial geometry at 0ps.

3.3. Conclusion

We have demonstrated that new mixed-perovskite solar cells based on $FA_{0.4}MA_{0.6}PbI_{2.9}Br_{0.1}$, whose composition is engineered to minimize the crystal distortion, exhibit improved photovoltaic performance and stability compared to widely-used $MAPbI_3$ based devices. These cells incorporate C_{60} as ETL, which is advantageous over TiO_2 due to low-temperature processability, absence of hysteresis, and enhanced device stability. As a result, our best device have shown the PCE of 20.2%, the highest efficiency of all low-temperature processed perovskite solar cells.

We also demonstrated the degradation mechanism of $FAPbI_3$ material. In the case of $FAPbI_3$, the phase transition predominated over decomposition in the presence of water. However, in the case of low relative humidity condition, $FAPbI_3$ was decomposed by trapped charges. In particular, in AIMD simulation, we found the strong interaction between FA^+ cation and H_2O molecule which may induces the phase transition. Cs-doped $FAPbI_3$ was much slowly degraded than pure $FAPbI_3$ because Cs^+ cation stabilize the cubic structure. In the presence of oxygen, the phase transition of $FAPbI_3$ was suppressed and the decomposition of $FAPbI_3$ predominated. In this case, the degradation of $FAPbI_3$ occurred only when there were

trapped charges. It was predicted that the routes of degradation of $FAPbI_3$ were different from $MAPbI_3$.

3.4. Experimental method

Solution preparation. All solutions were prepared in the nitrogen-filled glove box. For the $MAPbI_3$ solution, equimolar amounts of metyhlammoium iodide (MAI), PbI_2, and dimethylsulfoxide (DMSO) (i.e., 159 mg of MAI (Xi'an Polymer Light Technology), 461 mg of PbI_2 (Alfa Aesar), and 78 mg of DMSO (Sigma-Aldrich)) were dissolved in 0.6 ml of dimethylformamide (DMF) (Sigma-Aldrich). Our multi-component perovskite solution was prepared in the likewise stoichiometric way, i.e., by dissolving 79.5 mg of MAI, 68.8 mg of formamidinium iodide (FAI), 11.2 mg of MABr, 461 mg of PbI_2, and equimolar DMSO in 0.6 ml of DMF. $FAPbI_3$ perovskite solution was prepared in the likewise stoichiometric way, i.e., by dissolving 172 mg of FAI, 461 mg of PbI_2, and 0.1ml N-Methyl-2-pyrrolidinone(NMP) in 0.6 ml of DMF. $FA_{0.95}Cs_{0.05}PbI_3$ was prepared in the likewise stoichiometric way, i.e., by dissolving 168.6 mg of FAI, 13mg of CsI, 461 mg of PbI_2, and 0.1ml N-Methyl-2-pyrrolidinone(NMP) in 0.6 ml of DMF.

To prepare the hole transport material (HTM) solution, 72.3 mg of Spiro-MeOTAD (Merk), 28.8 µl (26.6mg) of 4-tert-butyl pyridine (Sigma-Aldrich, 96%) and 17.5 µl of lithium bis(trifluoromethanesulfonyl)imide (Li-TFSI) solution (520 mg Li-

TSFI (Sigma-Aldrich) in 1 ml acetonitrile (Sigma–Aldrich, 99.8%)) were dissolved in 1 ml of chlorobenzene (Sigma-Aldrich).

Perovskite film & device fabrication. Indium tin oxide(ITO)-coated glass (AMG, 9.5Ω cm^{-2}, 25×25 mm^2) and pure glass (AMG, 25×25 mm^2) substrates were sequentially cleaned by sonication in acetone, isopropanol, and deionized water for 15 min each. All perovskite films were fabricated by Lewis base adduct method[3]. To fabricate a perovskite film, the prepared perovskite solution was coated on a pure glass substrate by spin-coating at 4000 rpm for 20 s with diehtyl ether dripping treatment. After spin-coating, the $MAPbI_3$ film was sequentially annealed at 65 ^oC for 1 min and 100 ^oC for 4 min. Our multi-component perovskite film was fabricated via the same method and annealed at 130 ^oC for 20 min. $FAPbI_3$ and $FA_{0.95}Cs_{0.05}PbI_3$ perovskite films ware fabricated via the same method and annealed at 150 ^oC for 20 min.To prepare the electron transport layer (ETL), a 35-nm-thick layer of C_{60} was deposited on the cleaned ITO glass substrate by using a vacuum thermal evaporator (<10^{-7} Torr) at the constant rate of 0.1 Å s^{-1}. After the C_{60} deposition, the perovskite layer was coated by the same process. The HTM solution was then coated on the ITO/C_{60}/perovskite substrate by spin-coating at 2000 rpm for 30 s. Finally, a 50-nm-thick layer of

gold was deposited on the HTM by using the same vacuum thermal evaporator at the constant rate of 0.3 Å s^{-1}.

Experimental setup for degradation test

The fully sealed rectangular parallelpiped (RP) chamber has an inner dimension of 35 mm width, 35 mm length, and 30 mm height. This chamber is made of stainless steel to prevent gas leakage except for the top with quartz windows that let light pass through. For ion generation and deposition, two connected chambers, each designated IG for ion generation and ID for ion deposition, were used. The IG chamber produces nitrogen ions by corona discharge that uses an asymmetric field to extract electrons from nitrogen molecules. The ions are then transported by the gas flow and deposited on the perovskite film by the electrostatic force exerted by a high negative voltage applied (–2 kV). The IG chamber is cylindrical in shape (30 mm in diameter, 35 mm in height) and made of transparent acrylic material so that corona discharge can be visually monitored. The ID chamber is also cylindrical in shape (50 mm in diameter, 60 mm in height) and made of stainless steel to block all incoming light. The two chambers are connected to the tee tube so that water molecules or oxygen molecules could be introduced from outside.

The rate of injected gas is controlled by a mass flow controller (MKS Instruments, MFC Controller 247D, MFC 1179A). We used highly purified gases of nitrogen (99.999%) and oxygen (99.995%). Dry air consists of 80% nitrogen and 20% oxygen. To inject water molecules, nitrogen gas was passed through a water bubbler and the relative humidity was monitored by a portable multifunction data-logger (Delta OHM, Data logger DO9847, Temp&Humidity probe HP474AC) at the center of the RP chamber and gas exit of ID chamber. The light soaking experiment was carried out under AM 1.5G one sun irradiation by using a 450 W xenon lamp (Oriel Sol3A) which was calibrated by standard Si photovoltaic cell (Rc-1000-TC-KG5-N, VLSI Standards).

Characterization

Absorption spectra measurements. The absorption spectra of perovskite films were measured by a UV-vis spectrophotometer (Agilent Technologies, Cary 5000) in the wavelength range from 400 to 850 nm.

J-V curve measurement. The photocurrent density-voltage characteristics of perovskite solar cells were measured by a solar

simulator with 450 W xenon lamp (Oriel Sol3A) and a current meter (Keithley 2400) under AM 1.5G one sun irradiation, in which the light source was calibrated by using standard Si photovoltaic cell (Rc-1000-TC-KG5-N, VLSI Standards). A metal mask with an aperture of 7.29 mm^2 was used in the measurements.

Computational details

All DFT calculations were performed with the Vienna *ab initio* simulation package (VASP, version 5.3.5),[50] and the results were visualized by the VESTA (visualization for electronic and structural analysis) and the VMD (Visual Melecular Dynamics) program[51,52]. The projector augmented wave (PAW) method[53,54] was used to describe the electron-ion interaction with the kinetic energy cutoff set to 520.0 eV for the plane waves. We used the Perdew-Burke-Ernzerhof (PBE) exchange-correlation functional[55] and weak van der Waals interactions were considered by the zero damping DFT-D3 method of Grimme[56]. We performed spin-unpolarized calculations for the neat, water-, and nitrogen-covered $FAPbI_3$ surface but spin-polarized calculations for the oxygen-covered $FAPbI_3$ surface to consider the triplet-state nature of the ground state oxygen. The Brillouin-zone was sampled with a Γ-centered (4 × 1 × 4) Monkhorst-Pack k-point grid for structural

relaxation and only a single Γ-point was used for the AIMD simulation. All AIMD simulations were performed in the canonical ensemble using Nosé thermostat with a temperature of 298 K. The total simulation time of each trajectory was 2 ps with a 2 fs time-step. The charge of molecules were obtained by summing atomic charges from Bader population analysis.[57]

We made the cubic crystal structure of $FAPbI_3$ at 25 ℃ ($a = b = c$ = 6.36 Å).[81] Initial geometries for AIMD simulation were prepared by placing 4 H_2O, 2 O_2, or a null layer at appropriate positions of the $FAPbI_3$ surface. After the initial relaxation in the neutral state, the simulation started with a net charge of +1, 0, or −1 in the unit cell by ejecting (+1) or injecting (−1) an electron. In all surface relaxations and simulations, two $FAPbI_3$ units at the bottom of the unit cell were rigidly fixed while all other atoms that compose the upper two $FAPbI_3$ units and the adsorbates were allowed to move.

Acknowledgement

This work was supported by the Global Frontier R&D Program on Center for Multiscale Energy System funded by the National Research Foundation under the Ministry of Science, ICT, and Future Planning, Korea.

The research data of Chapter 2 and 3 are the result on the collaboration with Namyoung Ahn (Seoul National University, Feb, 2018) and Eunhak Lim(Seoul National University), therefore it may include similar (or possibly same) content in dissertation of Namyoung Ahn and Eunhak Lim. Some research data of this thesis have been published in Nature Communications (*Nature Communications*, **7**, 13422, 2016). In addition, the rest of research results of this thesis will be published in the academic journals.

References

1 Jacobson, M. Z. & Delucchi, M. A. Providing all global energy with wind, water, and solar power, Part I: Technologies, energy resources, quantities and areas of infrastructure, and materials. *Energy Policy* **39**, 1154-1169 (2011).

2 Kojima, A., Teshima, K., Shirai, Y. & Miyasaka, T. Organometal Halide Perovskites as Visible-Light Sensitizers for Photovoltaic Cells. *Journal of the American Chemical Society* **131**, 6050-6051 (2009).

3 Ahn, N. *et al.* Highly Reproducible Perovskite Solar Cells with Average Efficiency of 18.3% and Best Efficiency of 19.7% Fabricated via Lewis Base Adduct of Lead(II) Iodide. *Journal of the American Chemical Society* **137**, 8696-8699 (2015).

4 Yoon, J. *et al.* Superflexible, high-efficiency perovskite solar cells utilizing graphene electrodes: towards future foldable power sources. *Energy & Environmental Science* **10**, 337-345 (2017).

5 Jeon, N. J. *et al.* Compositional engineering of perovskite materials for high-performance solar cells. *Nature* **517**, 476-480 (2015).

6 Saliba, M. *et al.* Cesium-containing triple cation perovskite solar cells: improved stability, reproducibility and high efficiency. *Energy & Environmental Science* **9**, 1989-1997 (2016).

7 Bu, T. *et al.* A novel quadruple-cation absorber for universal hysteresis elimination for high efficiency and stable perovskite solar cells. *Energy & Environmental Science* **10**, 2509-2515 (2017).

8 Lee, J.-W. *et al.* Formamidinium and Cesium Hybridization for Photo- and Moisture-Stable Perovskite Solar Cell. *Advanced Energy Materials* **5**, 1501310-n/a (2015).

9 Lee, J.-W. *et al.* Tuning Molecular Interactions for Highly Reproducible and Efficient Formamidinium Perovskite Solar Cells via Adduct Approach. *Journal of the American Chemical Society* **140**, 6317-6324 (2018).

10 Jung, H. S. & Park, N.-G. Perovskite Solar Cells: From Materials to Devices. *Small* **11**, 10-25 (2014).

11 You, J. *et al.* Improved air stability of perovskite solar cells via solution-processed metal oxide transport layers. *Nature Nanotechnology* **11**, 75 (2015).

12 Malinauskas, T. *et al.* Enhancing Thermal Stability and Lifetime of Solid-State Dye-Sensitized Solar Cells via Molecular Engineering of the Hole-Transporting Material Spiro-OMeTAD. *ACS Applied Materials & Interfaces* **7**, 11107-11116 (2015).

13 Sanchez, R. S. & Mas-Marza, E. Light-induced effects on Spiro-OMeTAD films and hybrid lead halide perovskite solar cells. *Solar Energy Materials and Solar Cells* **158**, 189-194 (2016).

14 Kato, Y. *et al.* Silver Iodide Formation in Methyl Ammonium Lead Iodide Perovskite Solar Cells with Silver Top Electrodes. *Advanced Materials Interfaces* **2**, 1500195 (2015).

15 Leguy, A. M. A. *et al.* Reversible Hydration of CH3NH3PbI3 in Films, Single Crystals, and Solar Cells. *Chemistry of Materials* **27**, 3397-3407 (2015).

16 Aristidou, N. *et al.* The Role of Oxygen in the Degradation of Methylammonium Lead Trihalide Perovskite Photoactive Layers. *Angew Chem Int Ed Engl* **54**, 8208-8212 (2015).

17 Ahn, N. *et al.* Trapped charge-driven degradation of perovskite solar cells. *Nature Communications* **7**, 13422 (2016).

18 Leijtens, T. *et al.* Stability of Metal Halide Perovskite Solar Cells. *Advanced Energy Materials* **5**, 1500963-n/a (2015).

19 Yang, J., Siempelkamp, B. D., Liu, D. & Kelly, T. L. Investigation of CH3NH3PbI3 Degradation Rates and Mechanisms in Controlled Humidity Environments Using in Situ Techniques. *ACS Nano* **9**, 1955-1963 (2015).

20 Ito, S., Tanaka, S., Manabe, K. & Nishino, H. Effects of Surface Blocking Layer of Sb2S3 on Nanocrystalline TiO2 for CH3NH3PbI3 Perovskite Solar Cells. *The Journal of Physical Chemistry C* **118**, 16995-17000 (2014).

21 Yoon, H., Kang, S. M., Lee, J.-K. & Choi, M. Hysteresis-free low-temperature-processed planar perovskite solar cells with 19.1% efficiency. *Energy & Environmental Science* **9**, 2262-2266 (2016).

22 Anaraki, E. H. *et al.* Highly efficient and stable planar perovskite solar cells by solution-processed tin oxide. *Energy & Environmental Science* **9**, 3128-3134 (2016).

23 Leijtens, T. *et al.* Mapping Electric Field-Induced Switchable Poling and Structural Degradation in Hybrid Lead Halide Perovskite Thin Films. *Advanced Energy Materials* **5**, 1500962-n/a (2015).

24 Bryant, D. *et al.* Light and oxygen induced degradation limits the operational stability of methylammonium lead triiodide perovskite solar cells. *Energy Environ. Sci.* **9**, 1655-1660 (2016).

25 Aristidou, N. *et al.* Fast oxygen diffusion and iodide defects mediate oxygen-induced degradation of perovskite solar cells. *Nat Commun* **8**, 15218 (2017).

26 Nazarenko, O., Yakunin, S., Morad, V., Cherniukh, I. & Kovalenko, M. V. Single crystals of caesium formamidinium lead halide perovskites: solution growth and gamma dosimetry. *Npg Asia Materials* **9**, e373 (2017).

27 Chen, W. *et al.* Efficient and stable large-area perovskite solar cells

with inorganic charge extraction layers. *Science* **350**, 944 (2015).

28 Shin, S. S. *et al.* Colloidally prepared La-doped BaSnO3 electrodes for efficient, photostable perovskite solar cells. *Science* **356**, 167-171 (2017).

29 You, J. *et al.* Improved air stability of perovskite solar cells via solution-processed metal oxide transport layers. **11**, 75 (2015).

30 Christians, J. A., Miranda Herrera, P. A. & Kamat, P. V. Transformation of the Excited State and Photovoltaic Efficiency of CH3NH3PbI3 Perovskite upon Controlled Exposure to Humidified Air. *Journal of the American Chemical Society* **137**, 1530-1538 (2015).

31 Habisreutinger, S. N. *et al.* Carbon Nanotube/Polymer Composites as a Highly Stable Hole Collection Layer in Perovskite Solar Cells. *Nano Letters* **14**, 5561-5568 (2014).

32 Tong, C.-J. *et al.* Uncovering the Veil of the Degradation in Perovskite CH3NH3PbI3 upon Humidity Exposure: A First-Principles Study. *The Journal of Physical Chemistry Letters* **6**, 3289-3295 (2015).

33 Divitini, G. *et al.* In situ observation of heat-induced degradation of perovskite solar cells. **1**, 15012 (2016).

34 Mei, A. *et al.* A hole-conductor–free, fully printable mesoscopic perovskite solar cell with high stability. *Science* **345**, 295 (2014).

35 Chang, J., Lawless, P. A. & Yamamoto, T. Corona discharge processes. *IEEE Transactions on Plasma Science* **19**, 1152-1166 (1991).

36 Kim, H.-S. *et al.* Control of I–V Hysteresis in CH3NH3PbI3 Perovskite Solar Cell. *The Journal of Physical Chemistry Letters* **6**, 4633-4639 (2015).

37 Chen, B., Yang, M., Priya, S. & Zhu, K. Origin of J–V Hysteresis

in Perovskite Solar Cells. *The Journal of Physical Chemistry Letters* **7**, 905-917 (2016).

38 Tress, W. *et al.* Understanding the rate-dependent J-V hysteresis, slow time component, and aging in CH3NH3PbI3 perovskite solar cells: the role of a compensated electric field. *Energy & Environmental Science* **8**, 995-1004 (2015).

39 Schmidt-Mende, L. & Grätzel, M. TiO2 pore-filling and its effect on the efficiency of solid-state dye-sensitized solar cells. *Thin Solid Films* **500**, 296-301 (2006).

40 Liang, P.-W., Chueh, C.-C., Williams, S. T. & Jen, A. K. Y. Roles of Fullerene-Based Interlayers in Enhancing the Performance of Organometal Perovskite Thin-Film Solar Cells. *Advanced Energy Materials* **5**, 1402321-n/a (2015).

41 Kim, H.-S. *et al.* Mechanism of carrier accumulation in perovskite thin-absorber solar cells. **4**, 2242 (2013).

42 Lin, Q., Armin, A., Nagiri, R. C. R., Burn, P. L. & Meredith, P. Electro-optics of perovskite solar cells. **9**, 106 (2014).

43 Juarez-Perez, E. J. *et al.* Photoinduced Giant Dielectric Constant in Lead Halide Perovskite Solar Cells. *The Journal of Physical Chemistry Letters* **5**, 2390-2394 (2014).

44 Frost, J. M. *et al.* Atomistic Origins of High-Performance in Hybrid Halide Perovskite Solar Cells. *Nano Letters* **14**, 2584-2590 (2014).

45 Leguy, A. M. A. *et al.* Reversible Hydration of CH3NH3PbI3in Films, Single Crystals, and Solar Cells. *Chemistry of Materials* **27**, 3397-3407 (2015).

46 Pearson, A. J. *et al.* Oxygen Degradation in Mesoporous Al2O3/CH3NH3PbI3-xClxPerovskite Solar Cells: Kinetics and Mechanisms. *Advanced Energy Materials* **6**, 1600014 (2016).

47 Li, Y. *et al.* High-efficiency robust perovskite solar cells on

ultrathin flexible substrates. *Nature Communications* **7**, 10214 (2016).

48 Niu, G. *et al.* Study on the stability of CH3NH3PbI3 films and the effect of post-modification by aluminum oxide in all-solid-state hybrid solar cells. *Journal of Materials Chemistry A* **2**, 705-710 (2014).

49 Weber, A. & Mcginnis, E. A. The Raman Spectrum of Gaseous Oxygen. *Journal of Molecular Spectroscopy* **4**, 195-200 (1960).

50 Hafner, J. Ab-initio simulations of materials using VASP: Density-functional theory and beyond. *J Comput Chem* **29**, 2044-2078 (2008).

51 Momma, K. & Izumi, F. VESTA 3for three-dimensional visualization of crystal, volumetric and morphology data. *Journal of Applied Crystallography* **44**, 1272-1276 (2011).

52 Humphrey, W., Dalke, A. & Schulten, K. VMD: visual molecular dynamics. *J Mol Graph* **14**, 33-38, 27-38 (1996).

53 Blöchl, P. E. Projector augmented-wave method. *Physical Review B* **50**, 17953-17979 (1994).

54 Kresse, G. & Joubert, D. From ultrasoft pseudopotentials to the projector augmented-wave method. *Physical Review B* **59**, 1758-1775 (1999).

55 John P. Perdew, K. B., Matthias Ernzerhof. Generalized Gradient Approximation Made Simple. *Physical review letters* **77**, 4 (1996).

56 Grimme, S., Antony, J., Ehrlich, S. & Krieg, H. A consistent and accurate ab initio parametrization of density functional dispersion correction (DFT-D) for the 94 elements H-Pu. *J Chem Phys* **132**, 154104 (2010).

57 Henkelman, G., Arnaldsson, A. & Jónsson, H. A fast and robust algorithm for Bader decomposition of charge density.

Computational Materials Science **36**, 354-360 (2006).

58 Baikie, T. *et al.* Synthesis and crystal chemistry of the hybrid perovskite (CH3NH3)PbI3 for solid-state sensitised solar cell applications. *Journal of Materials Chemistry A* **1**, 5628 (2013).

59 Yang, W. S. *et al.* Iodide management in formamidinium-lead-halide–based perovskite layers for efficient solar cells. *Science* **356**, 1376 (2017).

60 Kim, H.-S. *et al.* Lead Iodide Perovskite Sensitized All-Solid-State Submicron Thin Film Mesoscopic Solar Cell with Efficiency Exceeding 9%. **2**, 591 (2012).

61 Michael M. Lee, J. T., Tsutomu Miyasaka, Takurou N. Murakami, Henry J. Snaith. Efficient hybrid solar cells based on meso-superstructured organomatal halide perovskites. *Science* **338**, 5 (2012).

62 Bi, D. *et al.* Polymer-templated nucleation and crystal growth of perovskite films for solar cells with efficiency greater than 21%. *Nature Energy* **1**, 16142 (2016).

63 Eames, C. *et al.* Ionic transport in hybrid lead iodide perovskite solar cells. *Nat Commun* **6**, 7497 (2015).

64 Amat, A. *et al.* Cation-induced band-gap tuning in organohalide perovskites: interplay of spin-orbit coupling and octahedra tilting. *Nano Lett* **14**, 3608-3616 (2014).

65 Berhe, T. A. *et al.* Organometal halide perovskite solar cells: degradation and stability. *Energy Environ. Sci.* **9**, 323-356 (2016).

66 Leijtens, T. *et al.* Overcoming ultraviolet light instability of sensitized TiO(2) with meso-superstructured organometal tri-halide perovskite solar cells. *Nat Commun* **4**, 2885 (2013).

67 Wang, S., Jiang, Y., Juarez-Perez, Emilio J., Ono, Luis K. & Qi, Y. Accelerated degradation of methylammonium lead iodide

perovskites induced by exposure to iodine vapour. *Nature Energy* **2**, 16195 (2016).

68 Li, Z. *et al.* Stabilizing Perovskite Structures by Tuning Tolerance Factor: Formation of Formamidinium and Cesium Lead Iodide Solid-State Alloys. *Chemistry of Materials* **28**, 284-292 (2016).

69 Noh, J. H., Im, S. H., Heo, J. H., Mandal, T. N. & Seok, S. I. Chemical management for colorful, efficient, and stable inorganic-organic hybrid nanostructured solar cells. *Nano Lett* **13**, 1764-1769 (2013).

70 Bi, D. *et al.* Efficient luminescent solar cells based on tailored mixed-cation perovskites. *Science Advances* **2** (2016).

71 Yang, W. S. *et al.* High-performance photovoltaic perovskite layers fabricated through intramolecular exchange. *Science* **348**, 1234 (2015).

72 Koh, T. M. *et al.* Formamidinium-Containing Metal-Halide: An Alternative Material for Near-IR Absorption Perovskite Solar Cells. *The Journal of Physical Chemistry C* **118**, 16458-16462 (2014).

73 McMeekin, D. P. *et al.* A mixed-cation lead mixed-halide perovskite absorber for tandem solar cells. *Science* **351**, 151 (2016).

74 Shannon, R. Revised effective ionic radii and systematic studies of interatomic distances in halides and chalcogenides. *Acta Crystallographica Section A* **32**, 751-767 (1976).

75 Cohen, B. N., Labarca, C., Davidson, N. & Lester, H. A. Mutations in M2 alter the selectivity of the mouse nicotinic acetylcholine receptor for organic and alkali metal cations. *The Journal of General Physiology* **100**, 373 (1992).

76 Dimesso, L., Quintilla, A., Kim, Y. M., Lemmer, U. & Jaegermann, W. Investigation of formamidinium and guanidinium lead tri-iodide powders as precursors for solar cells. *Materials Science and*

Engineering: B **204**, 27-33 (2016).

77 Green, M. A., Ho-Baillie, A. & Snaith, H. J. The emergence of perovskite solar cells. *Nature Photonics* **8**, 506 (2014).

78 Wang, Y. *et al.* Density functional theory analysis of structural and electronic properties of orthorhombic perovskite CH3NH3PbI3. *Phys Chem Chem Phys* **16**, 1424-1429 (2014).

79 Rajendra Kumar, G. *et al.* Phase transition kinetics and surface binding states of methylammonium lead iodide perovskite. *Phys Chem Chem Phys* **18**, 7284-7292 (2016).

80 Stoumpos, C. C., Malliakas, C. D. & Kanatzidis, M. G. Semiconducting Tin and Lead Iodide Perovskites with Organic Cations: Phase Transitions, High Mobilities, and Near-Infrared Photoluminescent Properties. *Inorganic Chemistry* **52**, 9019-9038 (2013).

81 Weller, M. T., Weber, O. J., Frost, J. M. & Walsh, A. Cubic Perovskite Structure of Black Formamidinium Lead Iodide, α-[HC(NH2)2]PbI3, at 298 K. *The Journal of Physical Chemistry Letters* **6**, 3209-3212 (2015).

갇힌 전하에 의한 유무기 페로브스카이트 물질의 비가역적인 분해 현상 연구

서울대학교 대학원 기계항공공학부

곽 귀 성

요약

유무기 복합 페로브스카이트 결정은 뛰어난 광전특성을 가지고 있어 다양한 광전소자로 활용되고 있다. 특히 페로브스카이트 태양전지는 높은 효율과 저렴한 생산 가격으로 실리콘 태양전지를 대체 할 것으로 예상된다. 이런 페로브스카이트 태양전지의 상용화의 가장 큰 문제점은 낮은 안정성이다. 페로브스카이트 태양전지의 안정성이 부족한 데는 다양한 원인들이 있지만 가장 중요한 원인은 페로브스카이트 물질이 쉽게 분해가 일어난다는 것이다. 페로브스카이트 물질은 공기 중에서 빛을 조사해주면 매우 쉽게 분해가 진행될 뿐 아니라 다양한 요인들에 의해 분해가 진행되게 된다. 따라서 이런 페로브스카이트 물질의 비가역적인 분해현상에 대한 근본적인 원인과 분해과정을 명확하게 밝히는 것이 페로브스카이트 태양전지의 장기 안정성을 확보하는데 반드시 필요하다.

첫째, 페로브스카이트 태양전지에 가장 많이 사용되는 $CH_3NH_3PbI_3$(MAPbI$_3$) 물질의 분해현상에 대해서 연구하였다. 페로브스카이트 태양전지의 경우 전자전달층(Electron transport layer)을 바꿔주는 경우 효율, 히스테레시스, 분해경향성 등이

달라지는 것을 확인하였다. 이는 모두 전하의 거동에 의해서 나타나는 특성이므로 페로브스카이트 분해현상의 원인이 전하일 것이라 추측하였다. 이를 증명하기 위해서 빛이 없는 조건에서 전하를 주입해 주기 위해 코로나 방전법을 이용하였다. 코로나 방전법을 이용하여 주입해준 전하는 Kelvin Probe Force Microscopy와 PL을 이용하여 페로브스카이트 층으로 전달되는 것을 확인할 수 있었다. 이렇게 주입된 전하와 수분 또는 산소가 있는 조건에서 페로브스카이트 물질이 분해되는 것을 확인하였고, 페로브스카이트 층에서 빠져 나오지 못한 갇힌 전하들이 페로브스카이트 물질의 분해에 핵심적인 원인임을 증명하였다. 보다 이론적인 분해 메커니즘을 분석하기 위해 Density functional theory(DFT) 기반의 ab initio molecular dynamics(AIMD) 시뮬레이션을 진행하였다. 시뮬레이션의 결과 갇힌 전하가 없으면 아무런 현상도 일어나지 않았으나 갇힌 전하가 있을때에는 수분 또는 산소와 반응하여 페로브스카이트 결정이 무너지게 된다는 것을 확인할 수 있었다.

둘째, $MAPbI_3$ 가 아닌 다른 종류의 페로브스카이트 물질의 탐색 및 분해 현상에 대해 연구하였다. 골드슈미츠 팩터(Goldschmidt factor) 계산을 통해 $MAPbI_3$에서 유기 양이온 또는 할라이드 음이온을 바꿔주면 결정구조가 정방구조에서 입방구조 변할 수 있다. 입방구조의 경우 정방구조 보다 구조적 안정성이 뛰어나고 높은 효율을 가질 수 있다. 따라서 $CH_3NH_3^+(MA^+)$ 유기 양이온 대신 $CH((NH_2)_2)^+(FA^+)$ 유기 양이온을 사용하고 I^- 할라이드 음이온 대신 Br^- 할라이드 음이온을 사용하여 입방구조의 페로브스카이트 조성을 탐색하였다. 그 결과 20.2%의 효율을 가지면서 $MAPbI_3$에 비해 뛰어난 안정성을 가지는 $MA_{0.6}FA_{0.4}PbI_{2.9}Br_{0.1}$의 조성을 찾아내었다.

이 조성 역시 갇힌전하가 있는 경우 분해현상이 나타나는 것을 확인하였으나 특히 산소가 있는 경우 $MAPbI_3$에 비해 압도적으로 높은 안정성을 보이는 것을 확인했다.

최근 FA 유기양이온만을 활용하여 입방구조의 $FAPbI_3$ 물질이 높은 효율과 뛰어난 광 안정성으로 많이 활용되고 있다. 따라서 $FAPbI_3$의 분해현상 역시 연구를 진행하였다. $FAPbI_3$의 경우 수분이 많은 조건에서는 빠르게 입방구조에서 육방구조로 변하게 되는 것을 확인하였다. 하지만 빛을 조사해 주는 조건에서 산소를 주입하여 주면 결정이 분해되어 PbI_2 형태로 변하는 것을 확인하였다. 이러한 과정 역시 갇힌 전하에 의한 효과임을 코로나 방전법과 AIMD 시뮬레이션을 통하여 확인할 수 있었다

주요어: 페로브스카이트 태양 전지, 유무기 복합 페로브스카이트, 갇힌 전하, 전자전달층, 분해 메커니즘, 코로나 방전법, AIMD 시뮬레이션, 입방 구조, 혼합 조성 페로브스카이트

학번: 2013-20643

List of Publications

[1] N. Ahn[+], **K. Kwak**[+], M. S. Jang, H. Yoon, B. Y. Lee, J.-K Lee, P. V. Pikhitsa, J. Byun, M.Choi*"Trapped charge driven degradation of perovskite solar cells" *Nature Communications,* 7, 13422, (2016)

[2] **K. Kwak**[+], N. Ahn[+], E. Lim[+], J. Heo, B. Y. Lee, K. Bang, S.K. Kim*, M.Choi* ,"Atomistic mechanism for trapped-charge driven degradation of perovskite solar cells", *arXiv:1709.04130,* (2017)